J. Fluid Mech. (2010), *vol.* 644, *pp.* 61–95.
doi:10.1017/S0022112009992035

Simulations of shear instabilities in interfacial gravity waves

MICHAEL F. BARAD† AND OLIVER B. FRINGER

Environmental Fluid Mechanics Laboratory, Stanford University, Stanford, CA 94305-4020, USA

(Received 1 October 2008; revised 3 September 2009; accepted 7 September 2009)

An adaptive numerical method is employed to simulate shear instabilities in open-ocean internal solitary-like gravity waves. The method is second-order accurate, employs block-structured adaptive mesh refinement, solves the incompressible Navier–Stokes equations and allows for the simulation of all of the length scales of interest by dynamically tracking important regions with recursively-nested finer grids. Two-dimensional simulations are performed over a range of parameters, which allows us to assess the conditions under which the shear instabilities in the waves occur, including a method to evaluate the critical Richardson number for instability based on the bulk wave parameters. The results show that although the minimum Richardson number is well below the canonical value of 1/4 in all simulations, this value is not a sufficient condition for instability, but instead a much lower Richardson number of 0.1 is required. When the Richardson number falls below 0.1, shear instabilities develop and grow into two-dimensional billows of the Kelvin–Helmholtz type. A linear stability analysis with the Taylor–Goldstein equation indicates that an alternate criterion for instability is given by $\overline{\sigma}_i T_w > 5$, where $\overline{\sigma}_i$ is the growth rate of the instability averaged over T_w, the period in which parcels of fluid are subjected to a Richardson number of less than 1/4. A third criterion for instability requires that $L_w/L > 0.86$, where L_w is half the length of the region in which the Richardson number falls below 1/4 and L is the solitary wave half-width. An eigendecomposition of the rate-of-strain tensor is performed to show that the pycnocline thickness increases within the wave because of pycnocline-normal strain and not because of diffusion, which has important ramifications for stability. A three-dimensional simulation indicates that the primary instability is two-dimensional and that secondary, three-dimensional instabilities occur thereafter and lead to strong dissipation and mixing.

1. Introduction

Like surface gravity waves, internal gravity waves propagate until they dissipate, either in open water or at bathymetric features. Internal wave breaking at bathymetric features is often caused by wave shoaling in shallow water. Open-water internal wave breaking can be caused by the growth of shear instabilities at the pycnocline, similar to the Kelvin–Helmholtz type (Troy & Koseff 2005; Fructus *et al.* 2009). Both of these breaking mechanisms lead to enhanced turbulence. In the oceanic context there is strong evidence in support of the idea that internal wave turbulence results in mixed

† Email address for correspondence: barad@stanford.edu

fluid which flows into other regions of the ocean interior (Munk & Wunsch 1998; Thorpe 2004). It is also believed that internal waves dissipate a significant amount of energy in the world's oceans (Egbert & Ray 2000). Therefore, understanding the physical processes that govern internal wave dissipation is critical to understanding the detailed energy budget of the global climate system.

In the field, clear signatures of internal wave shear instabilities have rarely been observed, since fine-scale turbulent structure is difficult to measure. Recently, however, striking measurements of shear-induced decay of internal waves on the Oregon Shelf by Moum *et al.* (2003) shed new light on the poorly understood decay of internal waves in open water. The measurements depict trains of near-surface, solitary-like waves of depression that propagate in the absence of significant shoaling effects, with clear signatures of shear instabilities that are the primary source of turbulence and dissipation. Owing to a lack of high-resolution velocity data, Moum *et al.* (2003) used one-dimensional density profiles to infer fine-scale velocity structure with the assumption that streamlines were parallel to isopycnals. They found that 'explosively growing' shear instabilities are possible and are the likely source of the observed billows of the Kelvin–Helmholtz type. Various other researchers have measured field-scale shear instabilities (see, among others, Woods 1968; Armi & Farmer 1988; Gossard 1990; Marmorino 1990), yet none are as clearly of the Kelvin–Helmholtz type as those in Moum *et al.* (2003).

Dissipative bottom-trapped internal waves of elevation were studied by Hosegood, Bonnin & van Haren (2004), Klymak & Moum (2003) and Scotti & Pineda (2004), who measured bottom-trapped solibores in the Faeroe–Shetland Channel, in the Oregon shelf and near the Massachusetts coast, respectively, while Carter, Gregg & Lien (2005) observed highly nonlinear solitary waves of elevation that propagate towards the shelf break in Monterey Bay. While the generation mechanism for these waves is not yet clear, dissipation and mixing levels within them are orders of magnitude higher than surface solitary-like waves because of enhanced bottom-generated turbulence. Helfrich & Melville (2006) noted that the most significant types of internal wave dissipation are radiation damping, boundary shear, wave breaking/shoaling and shear instability. Radiation damping occurs when internal waves, propagating along a pycnocline, radiate energy by exciting new internal waves that travel into regions with weaker stratification. This problem was originally studied by Maslowe & Redekopp (1980) and has been studied numerically by Pereira & Redekopp (1980). Boundary shear dissipation of internal waves is caused by bottom boundary layers that act as a drag on the wave as has been studied by Diamessis & Redekopp (2006). When compared with observations, Helfrich & Melville (1986) successfully accounted for boundary shear in their one-dimensional numerical study. The shoaling, breaking and interaction of internal waves because of bathymetric features has received significant attention in the literature (see, among others, Cacchione & Wunsch 1974; Helfrich & Melville 1986; Ivey & Nokes 1989; Slinn & Riley 1998; Javam, Imberger & Armfield 1999; Michallet & Ivey 1999; Grue *et al.* 2000; Ivey, Winters & Silva 2000; Lamb 2002, 2003; Vlasenko & Hutter 2002; Legg & Adcroft 2003; Venayagamoorthy & Fringer 2007). Shear-instability-based internal wave dissipation typically occurs in the troughs (or crests) of interfacial waves when shear and stratification conditions are sufficient, i.e. when the shear effects are not stabilized by stratification.

Numerous methods exist to compute the velocity field and minimum Richardson number in internal solitary waves without solving the full set of Euler or Navier–Stokes equations. For example, Lamb (2002) employed the Dubriel–Jacotin–Long (DJL; Long 1956) equation to compute the flowfield in a stable solitary wave, and

Fructus *et al.* (2009) employed a fully nonlinear three-layer model (described in detail in Fructus & Grue 2004) to calculate the minimum Richardson number in their experiments on shear instabilities in interfacial solitary waves. While these methods are accurate, it is often desirable to obtain estimates of the minimum Richardson number within a solitary wave based on bulk wave parameters, as was done by Bogucki & Garrett (1993). They developed a scaling relationship to predict the critical amplitude of the wave at which the Richardson number in the pycnocline is 1/4. They focused on two-layer internal solitary waves in which the upper layer of thickness H_1 rests on a lower layer of thickness H_2, and the total depth is given by $D = H_1 + H_2$. They used a continuity approach to derive the velocity difference across the layers, such that

$$\Delta U \approx \frac{\alpha D c}{(H_1 + \alpha)(H_2 - \alpha)}, \tag{1.1}$$

where the shallow-water solitary internal wave phase speed is given by

$$c = c_0 \left[1 + \frac{\alpha(H_2 - H_1)}{2H_1 H_2}\right], \tag{1.2}$$

in which the phase speed of infinitely long, infinitesimally small waves is given by

$$c_0 = \left(g' \frac{H_1 H_2}{D}\right)^{1/2}, \tag{1.3}$$

with $g' = g\Delta\rho/\rho_0$ the reduced gravity and $\Delta\rho$ the density difference between the layers. The velocity difference given in (1.1) was then used in their expression for the Richardson number,

$$Ri \approx \frac{g'\delta_0}{(\Delta U)^2}, \tag{1.4}$$

with the assumption that Ri is constant across the finite-thickness δ_0 interface. For long, small-amplitude waves in a deep lower layer, $\alpha \ll H_1 \ll H_2$, Bogucki & Garrett (1993) showed that the critical amplitude at which $Ri = 1/4$ is given by $\alpha_c = 2(\delta_0 H_1)^{1/2}$. This is similar to the findings of Troy & Koseff (2005), who showed that the critical amplitude is also proportional to $\delta_0^{1/2}$ for long, progressive interfacial waves in deep water.

Two-dimensional steady parallel inviscid homogeneous shear flows are unstable to infinitesimal perturbations under Rayleigh's inflection point theorem (Rayleigh 1880), which states that a necessary condition for instability is that there must be at least one inflection point in the velocity profile. Fjortoft (1950) further generalized this theorem and showed that for instability, $U'''/U' < 0$ is also required at the inflection point, where U is the velocity profile and U''' and U' are its third and first derivatives, respectively. If these flows are stratified, then they are stable if $Ri > 1/4$ everywhere (Howard 1961; Miles 1963). However, as pointed out by Hazel (1972), $Ri < 1/4$ is not a sufficient condition for instability because it is possible to have a stable, stratified shear layer in which the Richardson number at the pycnocline is less than 1/4. Furthermore, the Richardson number above and below the pycnocline is identically zero but does not induce an instability. When the velocity and density profiles change in time, such as in internal gravity waves, the necessary condition for instability can be even lower. In laboratory experiments of breaking progressive interfacial gravity waves, Troy & Koseff (2005) showed that instability occurred when $Ri < 0.075 \pm 0.035$, while in numerical experiments Fringer & Street (2003) showed that $Ri < 0.13$. Fructus *et al.* (2009) obtained a similar value of $Ri < 0.092 \pm 0.016$ for laboratory experiments

on interfacial solitary waves. Because of the large scatter in the critical Richardson number for instability, Fructus *et al.* (2009) have pointed out that a sharper criterion for instability requires the width of the region in solitary waves in which $Ri < 1/4$ to be 86 % of the wavelength of the solitary wave. Troy & Koseff (2005) used the Taylor–Goldstein equation to derive another criterion for instability in progressive waves that requires $\overline{\sigma}_i T_w > 5$, where $\overline{\sigma}_i$ is the growth rate of the instabilities averaged over T_w, the time in which a parcel of fluid is subjected to $Ri < 1/4$. This implies that a sufficient condition for instability requires that the time scale of the instability must be of the order of the time scale in which it is subjected to destabilizing shear.

Many researchers have used numerical simulations to study two-dimensional and three-dimensional shear instabilities evolving into decaying turbulence, and most studies have focused on billows of the Kelvin–Helmholtz type and the associated mixing. Werne & Fritts (1999) carried out three-dimensional simulations to study the evolution of Kelvin–Helmholtz billows, while Smyth & Moum (2000) performed three-dimensional simulations to study the turbulence and mixing associated with breaking of Kelvin–Helmholtz billows. They found that a significant amount of anisotropy at all turbulent scales of motion exists during three-dimensional billow breaking. To assess mixing efficiency, Caulfield & Peltier (2000) studied the mixing transition of saturated Kelvin–Helmholtz billows, including three-dimensional investigations of both a 'hyperbolic' instability and a convective destabilization for stratified as well as homogeneous shear flows.

To date, no numerical simulations of breaking open-ocean internal gravity waves have been presented in the literature. This is because accurate simulation of field-scale oceanic internal wave shear instabilities is extremely difficult. The numerical method must not only capture a large range of physical scales ($O(10$ km) to $O(10$ cm)), but it also must capture a virtually dissipation-free propagation process over long time scales. The key physical processes that must be simulated include the nonlinear evolution of long waves into kilometre-scale trains of solitary-like waves and the subsequent nonlinear growth of shear instabilities at the sub-metre scale. These processes can be accurately simulated with a two-dimensional approach insofar as understanding the development of the initial instabilities is concerned, because three-dimensional dynamics only become significant in the subsequent turbulent mixing stage after the two-dimensional instabilities have developed (see Fringer & Street 2003). Three-dimensional primary instabilities have been studied, but it was found that they only exist in a low-Reynolds-number ($Re < 300$) regime (see Smyth & Peltier 1990). Accurate simulation of these field-scale processes over such a large range of scales with today's computational resources, even in two dimensions, benefits tremendously from an adaptive numerical method.

Adaptive numerical methods for the solution of partial differential equations concentrate computational effort when and where it is most needed (see Almgren *et al.* 1998). For over two decades block-structured adaptive mesh refinement (AMR) has proven useful for overcoming limitations in computational resources and obtaining accuracy in problems outside of the internal gravity wave community (Berger & Oliger 1983; Berger & Colella 1989; Berger & Leveque 1989; Skamarock, Oliger & Street 1989; Skamarock & Klemp 1993; Bell *et al.* 1994, 2005; Wolfsberg & Freyberg 1994; Almgren *et al.* 1998; Barad & Colella 2005). Typically, in computational environmental fluid mechanics, mesh refinement work has focused on static, one-way nested refinement, in which finer grids are nested within coarser grids and these grids do not adapt in time. In one-way nesting, there is no feedback between the fine and

coarse grids, while in two-way nesting, the solution is fully coupled at the coarse–fine interface.

In this paper the focus is on improving the understanding of shear instabilities in solitary-like finite-depth interfacial internal gravity waves. Specifically, in §§ 1–3 the problem and simulation set-up are introduced for the two-dimensional simulations; in § 4 unstable waves are characterized by analysing the density evolution and normal straining; § 5 includes a linear stability analysis with the Taylor–Goldstein equation and compares the results with theoretical Richardson number scalings; § 6 compares the results with observations; § 7 considers three-dimensional effects.

2. Governing equations and numerical method

The physical processes that are studied in this paper contain spatial scales that span metres to kilometres, with temporal scales ranging from seconds to hours. Currently, the only way to accurately resolve this range of scales is to use parallel AMR, which discretizes the entire flow domain with coarse grids, and recursively finer nested grids adaptively track the evolution of internal waves. With AMR, one can zoom in on moving regions and accurately capture the important flow physics at multiple scales. The mathematical model tracks these moving regions with finer grids as they evolve throughout the spatial and temporal flow domain and expends computational resources only where and when they are needed.

The present study uses the fully adaptive block-structured two-way nested second-order accurate method of Barad, Colella & Schladow (2009). The method solves the variable-density incompressible Navier–Stokes equations and exhibits second-order accurate convergence in time and space. The governing equations are composed of a momentum balance, a divergence-free constraint and density conservation, such that

$$\boldsymbol{u}_t + (\boldsymbol{u}\cdot\nabla)\boldsymbol{u} = -\frac{\nabla p}{\rho} + \boldsymbol{g} + \nu\Delta\boldsymbol{u}, \tag{2.1}$$

$$\nabla\cdot\boldsymbol{u} = 0, \tag{2.2}$$

$$\rho_t + \boldsymbol{u}\cdot\nabla\rho = 0, \tag{2.3}$$

where $\boldsymbol{u}$ is the velocity vector; ρ is the density; $\boldsymbol{g} = -g\boldsymbol{k}$ is the gravitational acceleration in the vertical $\boldsymbol{k}$ direction; and ν is the kinematic viscosity. The Coriolis term and diffusion of density are intentionally omitted, and free-surface motions are eliminated with the rigid-lid approximation. Since density variations are small, and constant dynamic viscosity is assumed, a constant kinematic viscosity with the value $\nu = 10^{-6}\,\mathrm{m^2\,s^{-1}}$ is employed. In stratified shear flows the Reynolds number is typically defined as $Re_0 = \Delta U\delta_0/\nu$, where ΔU is the velocity difference across the shear layer with thickness δ_0 (Hogg & Ivey 2003). Others (for example see Lamb 2003) have used the Euler equations to study field-scale internal wave breaking, and therefore it is anticipated that using a physical value for ν is appropriate for the idealized simulations in this paper given that sufficient care is taken in determining the appropriate mesh spacing to resolve the scales of interest (see Troy & Koseff 2005 for a discussion of viscous effects on the decay of interfacial gravity waves). It is assumed that the physics governing the instabilities is independent of physical scalar diffusion, and hence it is ignored.

3. Simulation set-up

3.1. *Flow domain and parameter space*

Idealized simulations are performed in order to understand the nature of the internal wave shear instabilities observed on the Oregon Shelf by Moum *et al.* (2003). While figure 14 in that paper shows a striking image of billows of the Kelvin–Helmholtz type in a solitary wave, these large-scale billows are rarely observed (J. Moum, 2009, personal communication); much more common are the high-backscatter layers that form at solitary wave troughs and persist at the trailing edge of the solitary waves, as shown in figure 3 of that paper. These high-backscatter layers are ubiquitous in large-amplitude solitary waves and contribute to the mixing and dissipation induced by the waves, which was the premise behind the work of Bogucki & Garrett (1993). They assumed that interfacial solitary waves propagate into an undisturbed stratification with a pycnocline thickness that is thickened by shear instabilities that occur at some point within the wave where billows of the Kelvin–Helmholtz type originate. While Moum *et al.* (2003) hypothesized that the high-backscatter layers were due to the formation of Kelvin–Helmholtz billows that result from shear instabilities, the echosounder resolution was insufficient to resolve the details of their evolution. By employing high-resolution simulations through the use of AMR, we focus in the present paper on simulating the waves that were observed by Moum *et al.* (2003) and the instabilities along the pycnocline that they were unable to resolve with their measurements.

Based on (1.4) and the analysis of Bogucki & Garrett (1993), the Richardson number in solitary interfacial waves is a function of three parameters, namely H_1/H_2, or the ratio of the upper layer depth to the lower layer depth, δ_0/H_1, or the non-dimensional thickness of the pycnocline, and α/H_1, or the non-dimensional wave amplitude, such that

$$Ri = Ri\left(\frac{H_1}{H_2}, \frac{\delta_0}{H_1}, \frac{\alpha}{H_1}\right).$$

Assuming a critical Richardson number for instability, Ri_c, then implies that the non-dimensional critical amplitude for instability, α_c/H_1, can be written as

$$\frac{\alpha_c}{H_1} = \frac{\alpha_c}{H_1}\left(Ri_c, \frac{\delta_0}{H_1}, \frac{H_1}{H_2}\right).$$

In this paper we keep H_1/H_2 fixed and assess the effects of the non-dimensional interface thicknesses δ_0/H_1 on the critical amplitude and Richardson number for instability. This is similar to the objective of the work of Fringer & Street (2003) and Troy & Koseff (2005), who also studied the critical amplitude for instability in progressive waves by varying $k\delta_0$, where k is the wavenumber. Fructus *et al.* (2009) performed laboratory experiments to study instabilities in solitary interfacial waves and varied H_1/H_2 as well as δ_0/H_1. A discussion of the effects of H_1/H_2 is provided at the end of § 5.2.

Two-dimensional simulations are employed throughout this paper except in § 7, where we assess the effects of three-dimensionality. For the two-dimensional simulations, the simulation domain is of depth $D = 100\,\mathrm{m}$ and length 10 km. A right-propagating nonlinear wavetrain is generated by initializing a two-layer density field with a depression of the pycnocline near the left boundary and allowing it to steepen into a train of solitary-like waves that propagate into the domain. This initial density field is composed of two layers which differ in density by $\Delta\rho = 2\ \mathrm{kg\,m^{-3}}$ and are

Case	$k\delta_0$	α_0/H_1	δ_0/H_1	δ_0	$\Delta x_{\min}$	$\Delta y_{\min}$	$\Delta z_{\min}$
1F	0.013	2	0.05	1	0.3	–	0.2
2F	0.025	2	0.10	2	0.3	–	0.2
4F	0.050	2	0.20	4	0.3	–	0.2
8F	0.10	2	0.40	8	0.3	–	0.2
16F	0.20	2	0.80	16	0.3	–	0.2
4FSS	0.050	1.28	0.20	4	0.3	–	0.2
4FS	0.050	1.73	0.20	4	0.3	–	0.2
8FL	0.10	2.27	0.40	8	0.3	–	0.2
8FLL	0.10	2.62	0.40	8	0.3	–	0.2
4C	0.050	2	0.20	4	0.6	–	0.4
8C	0.10	2	0.40	8	0.6	–	0.4
4C3D	0.050	2	0.20	4	0.6	0.6	0.4

TABLE 1. Summary of the cases simulated in the present paper. The leading number in the case identifier indicates the interface thickness δ_0; 'C' indicates a coarser resolution; 'F' indicates a finer resolution; 'S' indicates a smaller initial wave; and 'L' indicates a larger initial wave. Case 4C3D is a three-dimensional simulation, while the rest are two-dimensional simulations. Here, δ_0, $\Delta x_{\min}$, $\Delta y_{\min}$ and $\Delta z_{\min}$ are in metres.

separated by a pycnocline with a thickness δ_0, such that at time $t = 0$,

$$\rho(x, z, t = 0) = \rho_0 + \frac{\Delta\rho}{2} \tanh\left[-m_0(z - \psi(x, t = 0))\right], \tag{3.1}$$

where $m_0 = 2\tanh^{-1}(\beta)/\delta_0$. The initial (Gaussian) shape of the isopycnal defined by $\rho = \rho_0 = 1025\ \mathrm{kg\,m^{-3}}$ is given by

$$\psi(x, t = 0) = H_2 - \alpha_0 \exp\left(-\frac{x^2}{\sigma^2}\right), \tag{3.2}$$

where the undisturbed elevation of the isopycnal is $H_2 = 80\,\mathrm{m}$; the amplitude of the initial depression is α_0; the Gaussian half-width is $\sigma = 500$ m; and $\beta = 0.99$, which implies that our interface thickness is defined by the '99 %' interface thickness, as was done by Fringer & Street (2003) and Troy & Koseff (2005). In this way, the interface thickness is defined such that $\rho(z = \psi + \delta_0/2) - \rho(z = \psi - \delta_0/2) = -\beta\Delta\rho$. In the present study the interface thickness is varied, such that $\delta_0 = [1, 2, 4, 8, 16]$ m. This range of interface thicknesses was selected because it is similar to the range of stratifications observed by Moum *et al.* (2003). The resulting $k\delta_0$ range ($0.013 < k\delta_0 < 0.20$), where $k = 2\pi/\lambda$ (and λ is the wavelength), is roughly the same as that studied by Troy & Koseff (2005) and smaller than that of Fringer & Street (2003). The range of δ_0/H_1 is slightly smaller than that of Fructus *et al.* (2009), who studied waves with $0.27 < \delta_0/H_1 < 3.67$. The amplitude of the initial depression was held constant at $\alpha_0 = 2H_1$ for all but four cases as depicted in table 1. The leading number in the case identifier indicates the interface thickness δ_0, while 'C' indicates a coarser resolution and 'F' indicates a finer resolution. The three-dimensional run is denoted 4C3D (as it has $\delta_0 = 4\,\mathrm{m}$ and has coarser resolution). As will be shown, case 4F yields billows of the Kelvin–Helmholtz type, while case 8F does not. Therefore, we simulated two more cases with $\delta_0 = 4\,\mathrm{m}$ (4FS and 4FSS) to show that a reduction in the amplitude leads to a stable wave and two more cases with $\delta_0 = 8\,\mathrm{m}$ (8FL and 8FLL) to show that an increase in the amplitude leads to an unstable wave.

For all runs, a rank-ordered train of solitary-like internal waves of depression forms, and the leading wave travels at approximately $c = 0.7\,\mathrm{m\,s^{-1}}$. We define the wavelength λ as twice the distance from the trough of the leading wave to the point at which the ρ_0 isopycnal is displaced by 5 % relative to the maximum displacement in the trough. For the waves in our simulations λ has a characteristic value of $\lambda_c = 500\,\mathrm{m}$, and we use this length to normalize the x-coordinate in our discussion because it represents a characteristic value that does not change significantly among the waves, and it is useful to demonstrate variability in wave width among the cases by non-dimensionalizing the horizontal coordinate with the same scale (e.g. figure 6). However, when referring to the time scale of the instability it is important to refer to L_w/L, which is the ratio of half the width of the region within the wave in which $Ri < 1/4$ to the wave half-width L, which does indeed vary among the waves. We non-dimensionalize the x-coordinate by L, rather than λ, in § 5.1 in which we present a linear stability analysis with the Taylor–Goldstein equation. We also define a characteristic time scale $T \equiv \lambda/c \approx 729\,\mathrm{s}$ as the time it takes for the leading wave to propagate over one characteristic wavelength. In what follows the characteristic wavenumber is $k = 2\pi/\lambda$, and the normalized trough-centred coordinate is defined as $x_w \equiv (x - x_t)/\lambda$, where x_t is the location of the trough of the leading wave. As expected (see the discussion in Phillips 1977), the speed of the leading wave is weakly dependent on the interface thickness δ_0. However, as will be shown, the interface thickness strongly affects the stability properties of the waves.

3.2. *Qualitative features of a simulation*

In this section the basic features of a non-breaking simulation are presented. (In the current paper 'non-breaking' implies no overturning billows or that the vertical density gradient everywhere remains negative, i.e. $\rho_z < 0$.) This is to provide an overview of the physics of a non-breaking wave with an emphasis on understanding the wide range of scales involved. Details of billow formation and breaking are discussed in more detail later in the paper. Figure 1 shows the nonlinear transformation of case 8C from an initial Gaussian of depression into a rank-ordered train of solitary-like nonlinear internal gravity waves after an evolution time of $t/T = 18.5$. The figure depicts individual AMR patches, each of which contains $O(10^5)$ grid cells. This run has an effective resolution (i.e. a single grid without AMR) of $256 \times 16\,384$ computational cells, while the finest two-dimensional runs in this paper (where $\Delta z = 0.2\,\mathrm{m}$) have an effective resolution of $512 \times 32\,768$ or over 16 million computational cells. For all runs, although numerous AMR grids are employed with varying resolution, all grid cells have a fixed aspect ratio of $\Delta x/\Delta z = L/64D = 1.5625$, which ensures accurate results and good conditioning for the elliptic pressure solver. Grid refinement is employed based on the ability of the grid to accurately resolve density gradients and vorticity, as in Barad *et al.* (2009).

At the start of the simulation the initial transformation is a lifting of the initial half-Gaussian of depression. This is followed by a nonlinear transformation in which the leading edge of the Gaussian translates to the right. Subsequently, nonlinear dispersion of wave energy leads to a break up into a train of solitary-like waves, whereby the largest wave propagates to the right followed by slightly slower and successively smaller waves. With minimal numerical dissipation (see § 3.3 for a discussion of numerical convergence), the waves grow in size until they become solitary-like waves that slowly decay because of dissipation, leading to a train of rank-ordered solitary-like waves, as depicted in figure 1(*b*).

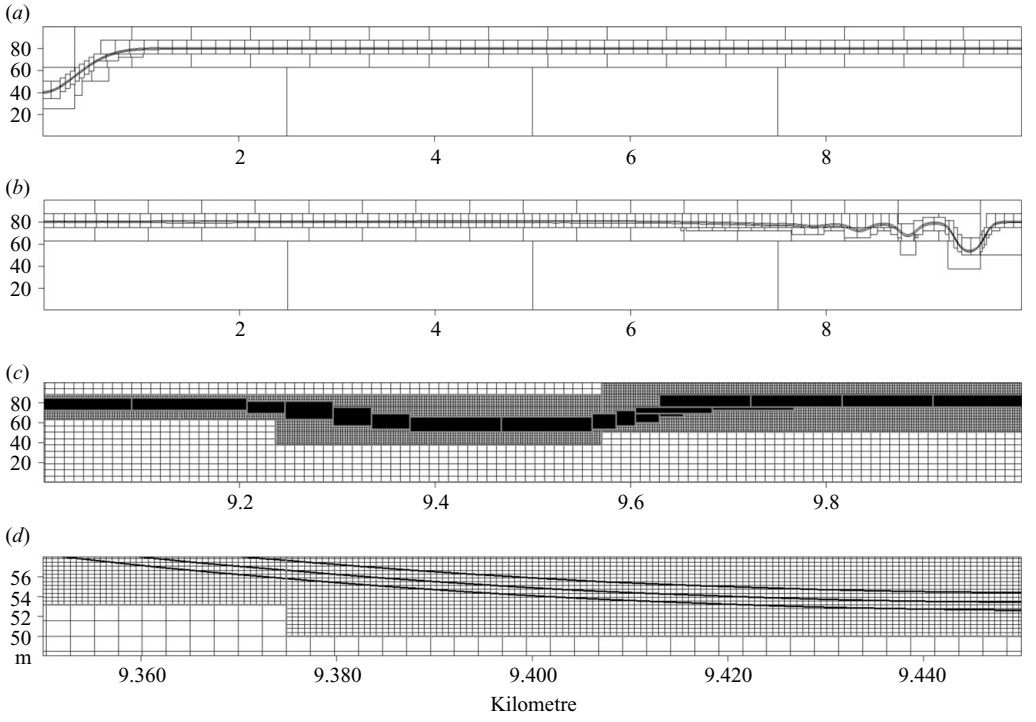

FIGURE 1. Density contour plots and mesh refinement patches for (*a*) initial conditions, $t/T = 0$, and (*b*) final state, $t/T = 18.5$. The contours are for $\rho = \rho_0$, $\rho_0 \pm \Delta\rho/4$, and this is case 8C (see table 1), with three levels of AMR. The vertical scale is in metres, while the horizontal scale is in kilometres; (*a*) and (*b*) have been horizontally compressed for visualization, while the actual physical aspect ratio of each computational cell is $\Delta x/\Delta z = L/64D = 1.5625$. (*c*) Depiction of the last 1 km of (*b*), at the real physical aspect ratio, with individual computational cells in black and block data structure patches in grey. (*d*) A view of (*c*) zoomed in by a factor of 10. The refinement ratio is 4 between all levels.

The analysis in the current paper focuses on the leading wave in the wavetrain that emerges from the Gaussian of depression, as this wave propagates into an undisturbed medium. The trailing waves behave similarly, although they are ignored in this paper, as their characteristics are slightly affected by the flow environment created by the waves that precede them. Figure 2(*a*) depicts the normalized horizontal position, x_t/λ, of the maximum depression of the ρ_0 isopycnal relative to its undisturbed depth, while figure 2(*b*) depicts the amplitude, α, of this depression normalized by the upper layer thickness, H_1. The amplitude is given by $\alpha \equiv D - z_t - H_1$, where z_t is the vertical location of the ρ_0 isopycnal at $x = x_t$. During the period $0 < t/T \leqslant 2$, the maximum amplitude decreases rapidly as the initial Gaussian of depression is uplifted because of the negative horizontal baroclinic pressure gradient. Then, during $2 < t/T \leqslant 4$, dispersion leads to the formation of a leading wave that emerges roughly at $t/T = 4$. The emergence of the leading wave is marked by a discontinuity in x_t when the position of maximum amplitude transitions from the location of maximum amplitude in the initial Gaussian to that in the leading wave that emerges. After it emerges and as is shown in figure 2(*b*), the amplitude of the leading wave continues to grow until it becomes essentially steady at roughly $t/T = 10$, after which time nonlinear steepening and dispersion are essentially in balance

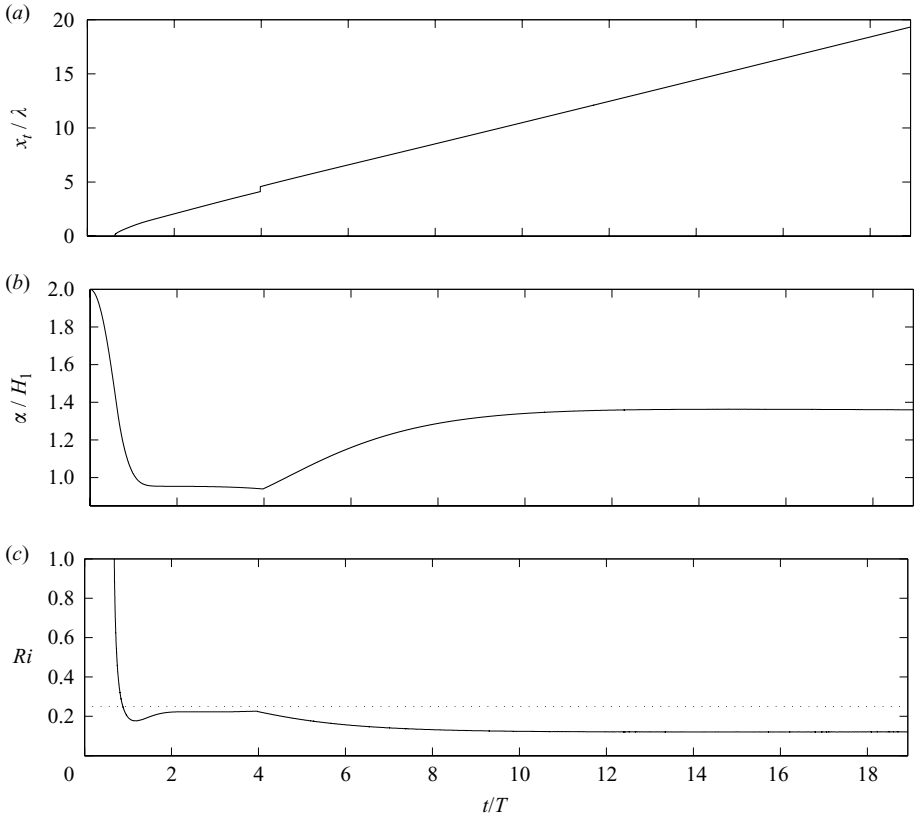

FIGURE 2. Time series of (*a*) the normalized horizontal position of maximum amplitude, x_t/λ, (*b*) the relative amplitude, α/H_1, and (*c*) the Richardson number at the trough of the leading wave for case 8F. The dotted line in (*c*) indicates $Ri = 1/4$.

in what forms the leading solitary-like wave that slowly decays because of weak dissipation.

Figure 2(*c*) depicts the gradient Richardson number, defined by

$$Ri \equiv \frac{N^2}{(u_z)^2} = -\frac{g}{\rho_0}\frac{\rho_z}{(u_z)^2}, \tag{3.3}$$

where N is the buoyancy frequency, ρ_z the vertical density gradient and u_z the vertical shear, all of which are defined at $(x, z) = (x_t, z_t)$. In (3.3) we use reference density ρ_0 which leads to the traditional form for the gradient Richardson number, even though the governing equations are non-Boussinesq. As described in § 4.3, the vertical gradient in density changes because of vertical strain which acts to decrease the buoyancy frequency at the wave trough. The reduction of the buoyancy frequency coupled with the development of strong vertical shear within the wave leads to marked changes in Ri as the leading solitary-like wave develops. This is apparent during the transition of the initial Gaussian wave of depression, which is marked by a sharp decrease in the Richardson number as the flows in the upper and lower layers accelerate in opposite directions. As the baroclinic pressure gradient subsides, the Richardson number increases during the period $1 < t/T \leqslant 2$, during which time the leading wave in the packet is forming. During $2 < t/T \leqslant 4$, the leading wave

continues to form, but Ri remains roughly constant because the shear is roughly constant at the location of maximum amplitude, even though the shear is decreasing to the left of this location and increasing to the right during the formation of the leading wave. Once the leading wave emerges roughly at $t/T = 4$, Ri decreases well below the canonical value of 1/4 until it reaches a steady value of 0.12 once the solitary-like wave forms at $t/T = 10$. Small oscillations that are present in these time series cannot be seen because they are too small to be detected at this scale. These oscillations do not lead to the formation of billows because they do not have sufficient time to grow, as discussed by Troy & Koseff (2005) and given in more detail in § 5.1.

3.3. *Accuracy*

In Barad & Fringer (2007) the same numerical method was used and the sensitivity of the solution to the mesh spacing was checked to determine the mesh spacing on the finest AMR level required to obtain a nearly grid-independent solution. This convergence study approach is common in the numerical solution of partial differential equations (e.g. see Bell, Colella & Glaz 1989). Resolution tests were conducted, and it was found that $D/\Delta z = 512$ (or $\Delta x = 0.3$ m and $\Delta z = 0.2$ m) was sufficient. In order to demonstrate convergence, time series of the relative amplitude of the leading wave were presented, along with time series of the Richardson number at the trough of this wave. As expected for a second-order accurate method, the time series converge to nearly grid-independent solutions. It was shown that poor grid resolution leads to the formation and rapid disintegration of the leading wave because of excessive numerical diffusion, which is marked by a rapid decay in wave amplitude. The simulations in Barad & Fringer (2007) indicate that the results in this paper are essentially grid independent.

4. Characteristics of unstable and breaking waves

4.1. *Density evolution*

To highlight large-scale wave density structure for a breaking solitary-like wave, figure 3 depicts the evolution of case 4F in time. As discussed in the previous section, the initial Gaussian of depression evolves into a train of rank-ordered solitary-like internal waves. The oscillations that appear at $t/T = 2$ are overturning billows that form as a result of a shear instability that originates at the location of maximum shear within the wave (see figure 4 for a detailed view of the billows). Initially, the maximum shear exists at the centre of the propagating Gaussian and the horizontal extent is of the order of the width of the Gaussian. However, as the wavetrain emerges, the patch of unstable fluid becomes confined to the trailing edge of the leading solitary-like wave. The strength of the billows grows as the amplitude, and hence magnitude of the shear, in the leading wave increases. This persists until $t/T \sim 10$, at which time the leading wave has evolved into a solitary-like wave in which billows form and are left in its wake because of a shear instability along the interface. These billows are the primary source of dissipation of the solitary-like wave and lead to a small decay in amplitude, which causes the slight decrease in the strength of the instabilities after $t/T \sim 10$ in figure 3.

Figure 4 depicts the detailed structure of the billows at the interface for the leading wave in case 4F at $t/T = 12$. As the strength of the shear grows from right to left near the trough and peaks at $x = x_t$, the flow becomes unstable to perturbations within the wave trough, leading to the formation of billows of the Kelvin–Helmholtz type towards the trailing edge of the wave. These are similar to the observations of Moum

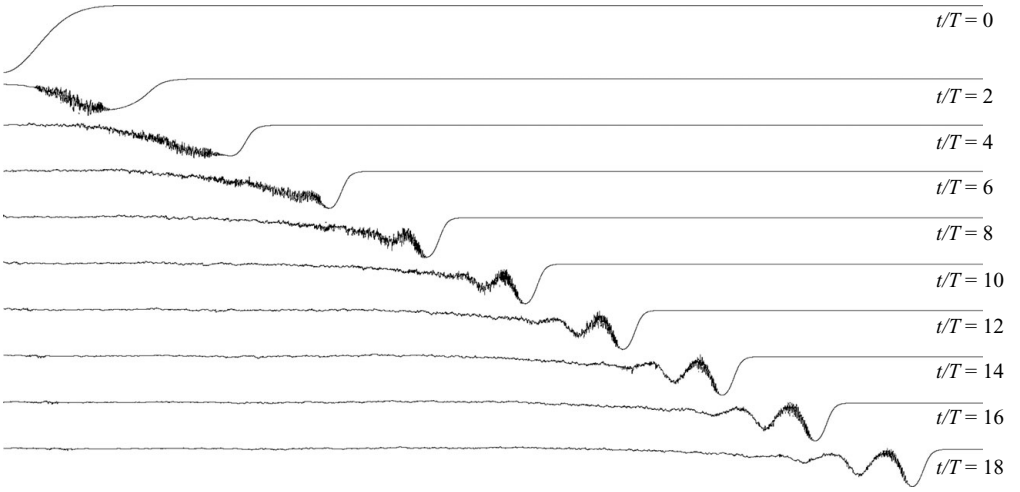

FIGURE 3. The development of a rank-ordered train of solitary-like waves for case 4F. The panels are ordered top to bottom with $t/T = [0, 2, 4, 6, 8, 10, 12, 14, 16, 18]$, and the contours are of $\rho = \rho_0$. The horizontal extent covers the entire domain of 10 km, while the vertical scale is the same for all contours, and for reference the amplitude of the initial Gaussian deflection is $\alpha_0 = 40$ m. A detailed view at time $t/T = 12$ is shown in figure 4.

et al. (2003), and we make comparisons with the observations in § 6. The size of the billows increases until the shear within the wave subsides, leaving behind a series of billows that interact with the velocity field in the trailing waves. Because the shear within these trailing waves is relatively small, the billows continue to decay, and as they decay and interact with one another the interface thickness increases because of enhanced diffusion. The primary billows have positive vorticity induced by the wave, while secondary billows of both positive and negative vorticity form, as expected for billows of the Kelvin–Helmholtz type. As will be seen in § 7, the three-dimensional case (case 4C3D) has similar two-dimensional pairing characteristics, and the flow is mostly two-dimensional. Figure 4 clearly indicates the multi-scale nature of this problem, since the billows are roughly 5 m in diameter, while the wave is roughly 500 m long. This is exceptionally difficult to simulate accurately, and no internal wave simulations that capture this range of scales have been presented in the literature to date.

Recalling the definition of Re_0 from § 2, for the simulations in this paper $\Delta U \approx 0.76\,\mathrm{m\,s^{-1}}$, and therefore $Re_0 \approx 7.6 \times 10^5$ for $\delta_0 = 1$ m and $Re_0 \approx 1.2 \times 10^7$ for $\delta_0 = 16$ m. As the $\delta_0 = 16$ m case is less likely to form billows because of the stratification, viscous effects (discussed in § 7) are even less significant for studying the shear instability in this high-Re_0 regime. Subsequent mixing will depend heavily on viscous decay, which is not the focus of this work. This is in agreement with the calculations of Haigh (1995) and Hogg & Ivey (2003), where they found viscous damping of high-frequency shear instabilities when $Re_0 \lesssim 100$.

4.2. *Wave amplitude*

Figure 5(*a*) depicts a time series of the maximum amplitude within the domain (α) normalized by the upper layer thickness (H_1), while figure 5(*b*) depicts the minimum Richardson number at the location of maximum amplitude. As discussed in § 3.2, a stable solitary-like wave emerges roughly at $t/T = 10$. High-frequency oscillations in the time series are indicative of instabilities that may grow and lead to the formation of Kelvin–Helmholtz billows (as are apparent in figures 4 and 6). These are clearly

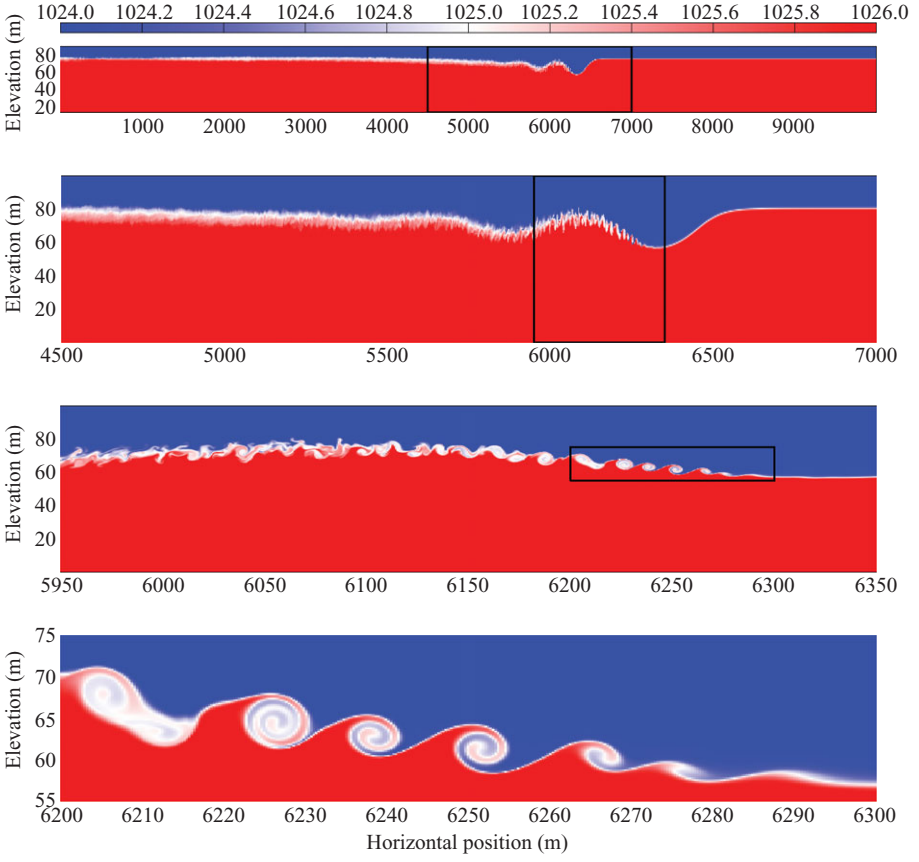

FIGURE 4. Detailed plot of the shear instability that has formed at $t/T = 12$ in the leading wave for case 4F. Contours depict density in $\mathrm{kg\,m^{-3}}$, and each plot is a zoomed-in view of the previous plot.

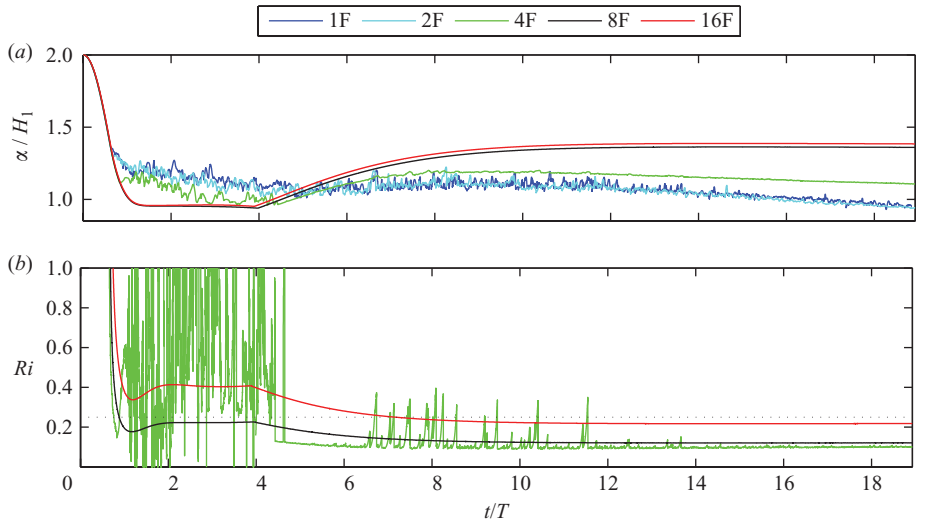

FIGURE 5. (*a*) Time series of the maximum amplitude of the leading wave trough and (*b*) the Richardson number at this location for cases 1F, 2F, 4F, 8F and 16F. Cases 1F and 2F are omitted from (*b*) for clarity.

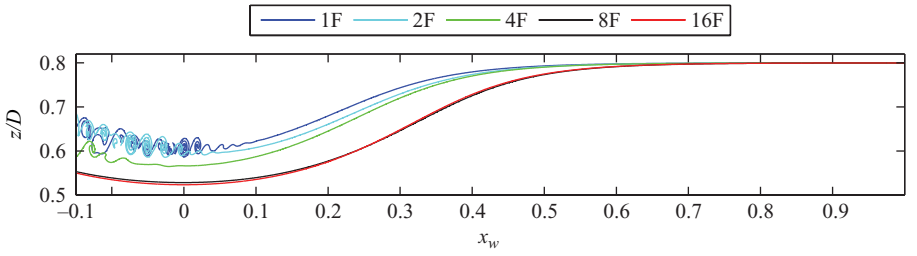

FIGURE 6. Distributions of the ρ_0 isopycnal within the waves at $t/T = 12$ for cases 1F, 2F, 4F, 8F and 16F.

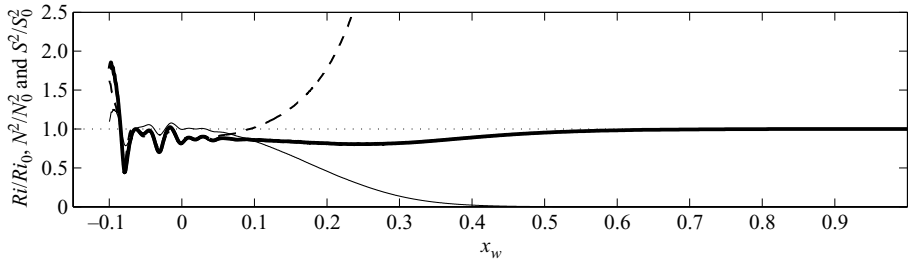

FIGURE 7. Relative magnitudes along the ρ_0 isopycnal of the Richardson number, Ri/Ri_0 (dashed line); the shear, S^2/S_0^2 (solid line); and the buoyancy frequency, N^2/N_0^2 (thick solid line). Data are from case 4F, at $t/T = 12$; S_0^2 and N_0^2 are the squares of the maximum vertical shear and the maximum buoyancy frequency, respectively, over $x_w > 0$; $Ri_0 = N_0^2/S_0^2$.

evident in the time series for $\delta_0/H_1 \leqslant 0.2$ (cases 1F, 2F and 4F in figure 5) while not strong for $\delta_0/H_1 \geqslant 0.4$ (cases 8F and 16F in figure 5). In particular, the time series with large high-frequency oscillations display a much stronger decay in wave amplitude than the more stable time series, which is because the billows grow by taking energy from the wave, and this reduces the wave amplitude. Dissipation and mixing of the billows occurs after sufficient billow growth (see figure 4). How much dissipation and mixing occurs depends on the strength of the instability. The magnitude of the amplitude decay increases for waves with thinner interfaces because of increased velocity shear. Because billows of the Kelvin–Helmholtz type also form during the formation of the waves (i.e. during the breakup of the initial Gaussian of depression; see figure 3 at $t/T = 2$), the amplitudes of the leading waves for small δ_0/H_1 are also substantially reduced. As discussed in Fringer & Street (2003), because these results are two-dimensional, the dissipation is under-predicted owing to the lack of the three-dimensional lateral instabilities that account for most of the mixing and dissipation. Furthermore, the mixing is purely numerical because we omit explicit numerical diffusion of density. A discussion of the three-dimensionality of the secondary instability is given in § 7.

4.3. *Normal straining*

Fluid parcels near the pycnocline during the passage of a solitary wave experience a marked increase in vertical shear while also experiencing a decrease in the vertical buoyancy frequency, as depicted in figure 7. The reduction in the buoyancy frequency results primarily from normal strain within the wave, rather than diffusion, which acts to increase the thickness of the pycnocline. The predominance of strain over diffusion has important ramifications for stability because an advection-dominated

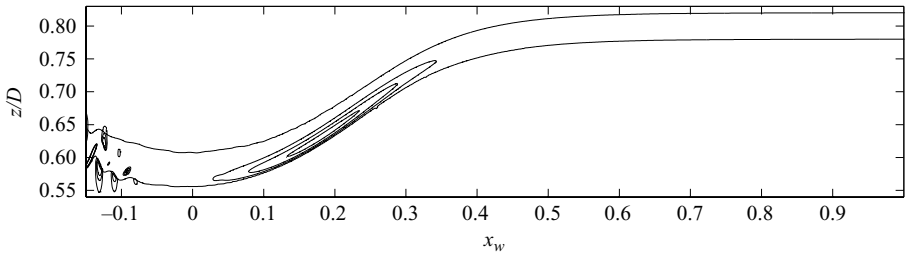

FIGURE 8. Vertical normal strain, w_z (where the contours are of 0.01, 0.02 and 0.03 s^{-1}), for case 4F at $t/T = 12$. The outer contours indicate the density interface as defined by $\rho = \rho_0 \pm \beta\Delta\rho/2$.

process enables parameterization of wave breaking that is independent of diffusion or mixing. To understand the influence of wave-induced strain on wave dynamics, we analyse the normal strain at $t/T = 12$ for case 4F, in the region of the leading edge of the first solitary wave in the wavetrain. Figure 8 shows a plot of the vertical normal strain (w_z), which is positive in the instability growth region. Values of w_z are largest near the lower boundary of the interface (the $\rho = \rho_0 + \beta\Delta\rho/2$ isopycnal) and gradually decrease vertically. The figure shows that rather than being compressed vertically as it moves downward, the interface expands vertically from an initial thickness of δ_0 to just over $(5/4)\delta_0$. As the wave propagates to the right, into the ambient fluid, fluid parcels are compressed horizontally ($u_x < 0$), which leads to vertical expansion as a result of incompressibility and hence positive vertical strain since $w_z > 0$.

To gain a better understanding of wave straining and the associated interface thickening process, data are extracted along the ρ_0 isopycnal and presented in figures 9 and 10. The along-contour straining is examined by computing the rate-of-strain tensor

$$\boldsymbol{E}_{i,j} = \frac{1}{2}\left(\frac{\partial u_i}{\partial x_j} + \frac{\partial u_j}{\partial x_i}\right) \tag{4.1}$$

and its eigendecomposition to determine the principle axes and rates of strain. For the two-dimensional incompressible flow equations, $\boldsymbol{E}$ is symmetric with two real eigenvalues which are of the same magnitude but have opposite signs, and trace($\boldsymbol{E}$) = 0 because of the divergence-free constraint. The rate-of-strain tensor is composed of terms in the velocity gradient tensor ($\partial u_i/\partial x_j$), which are shown in figure 9(b). The two eigenvectors of $\boldsymbol{E}$, $\vec{b}_1$ and $\vec{b}_2$, define the principal axes of strain, while the two eigenvalues λ_1 and λ_2 define the strain rates along these principal axes (Kundu 2002). The principal axes and strain rates can be visualized as ellipses in which the semi-major and semi-minor axes are aligned with the eigenvectors and stretched by the eigenvalues. These ellipses can be thought of as deformations of originally circular fluid elements, as depicted in figure 9(a). The ellipses are angled at roughly $\pi/4$ clockwise from the vertical. This $\pi/4$ rotation can be computed analytically from an eigendecomposition of a two-dimensional shear flow (e.g. $u = \tanh(z)$). Figure 10(a) shows the clockwise deviation from vertical for the ρ_0 isopycnal, the ($\pi/4$ adjusted) ellipse semi-major axis and the difference $\epsilon \equiv \theta_\rho - \theta_{strain} + \pi/4$, where, measured clockwise from vertical, θ_ρ is the angle of the ρ_0 isopycnal normal and $\theta_{strain} - \pi/4$ the angle of the strain-rate ellipses. In figure 10, ϵ is scaled by 8 for clarity.

The difference $|\epsilon| > 0$ induces a strain on the interface, and therefore if $\epsilon = 0$, then there is no net strain on the interface. When $\epsilon > 0$ net compression normal to the interface is expected (with stretching tangential), while for $\epsilon < 0$ net stretching

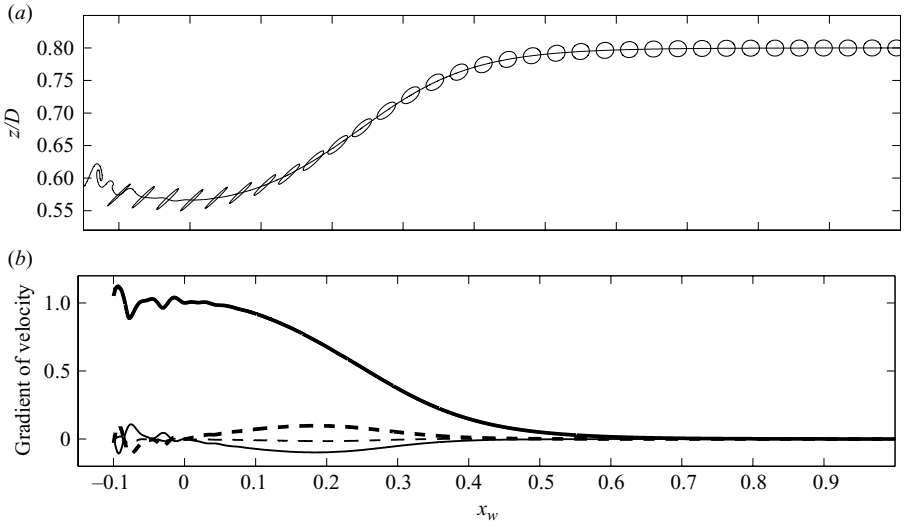

FIGURE 9. (*a*) The ρ_0 isopycnal with rate-of-strain principal-axes ellipses, where the ellipses represent deformations of circular fluid elements. While the contour is plotted with non-unit aspect ratio axes, the ellipses are plotted with an isotropic aspect ratio, and so when there is no strain they are circles. (*b*) Four components of the gradient of the velocity field, normalized by the magnitude of u_z at $x_w = 0$, where the lines represent $u_x/|u_z|$ (thin solid), $u_z/|u_z|$ (thick solid), $w_x/|u_z|$ (thin dashed) and $w_z/|u_z|$ (thick dashed). Note that the presence of billows can lead to $u_z/|u_z| > 1$ ahead of the wave crest. Data are from case 4F, at $t/T = 12$.

normal to the interface (with compression tangential) is expected. For $x_w > 0.3$, $\epsilon > 0$ and in this region isopycnal normal strain is expected (i.e. $\lambda \vec{b}_1 \cdot \nabla\rho/|\nabla\rho|$) to be net compressive. Progressing into the trough of the wave, for $0 < x_w < 0.3$, $\epsilon < 0$, and therefore the isopycnal normal strain is tensile. The eigenvalues, or stretching rates, are plotted in figure 10(*b*), where λ_1 is the eigenvalue corresponding to the semi-major axis and λ_2 is the one that corresponds to the semi-minor axis. The stretching rates increase moving into the wave (i.e. $x_w > 0.9$ and then $\rightarrow 0$) with a maximum magnitude roughly at $x_w = 0$. Combining figures 10(*a*) and 10(*b*), when $x_w > 0.3$ there is relatively weak compression of the isopycnals, while for $0 < x_w < 0.3$ there is strong isopycnal stretching. Figure 10(*c*) shows that the interface is in fact thickening as predicted by the eigendecomposition analysis. The eigendecomposition analysis predicts the precise location at which the interface rapidly thickens, at $x_w < 0.3$. It also describes precisely that the interface thickens because of normal straining rather than diffusion. A close inspection of figure 10(*c*) reveals that there is a very slight thickening of the interface for $x_w > 0.4$, which is probably diffusion at the front. This thickening is however countered at $0.3 < x_w < 0.4$ by isopycnal normal compression as predicted by the eigendecomposition analysis. Figure 10(*c*) also reveals that the interface thickens at roughly a linear rate for $-0.05 < x_w < 0.3$.

In summary, there are three regimes of normal straining. First, an essentially strain-free region with very minor interface thickening exists for $x_w > 0.4$. Second, a compressive region in which the interface is under weak compressive normal strain exists for $0.3 < x_w < 0.4$. This second region transitions to the third region when the straining switches from weak compression to strong expansion. The third region is one of linear interface thickening and occurs when $x_w < 0.3$. In this region, the expansion of the interface can be approximated by assuming that the interface at a horizontal

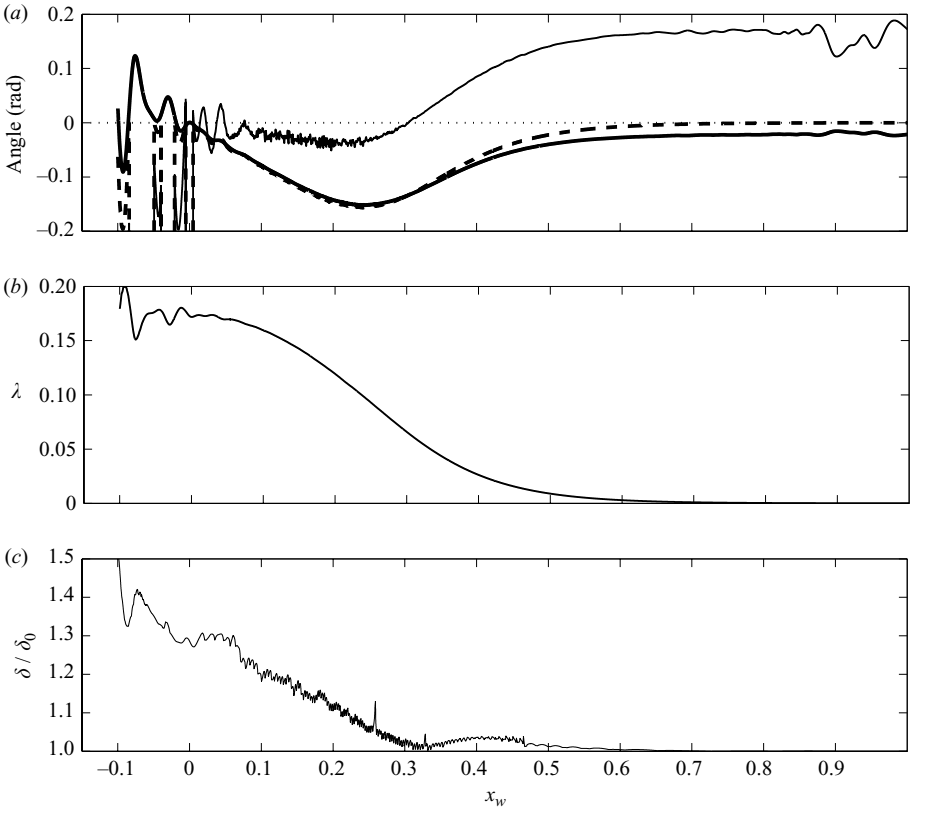

FIGURE 10. (*a*) The angle of the ρ_0 isopycnal normal from the vertical, θ_ρ (thick dashed line), and the angle of the strain rate ellipses, $\theta_{strain} - \pi/4$ (thick solid line), where the ellipse angle is rotated by $\pi/4$ counterclockwise (to align with the isopycnal orientation). The angles are measured in radians, where positive is clockwise from vertical. Also shown in (*a*) is the difference $\epsilon \equiv \theta_\rho - \theta_{strain} + \pi/4$, magnified by a factor of 8 for viewing (solid line). (*b*) The eigenvalues of the rate-of-strain tensor, λ_1 (note that $\lambda_1 = -\lambda_2$), and (*c*) the normalized interface thickness, δ/δ_0. Data are from case 4F, at $t/T = 12$.

location in space undergoes vertical strain because of a time-varying vertical velocity field. If δ_s is the thickness of the interface after undergoing vertical strain for half a wave period (i.e. at $x_w = 0$), then assuming that the effects of lateral strain are small,

$$\delta_s \approx \delta_0 + \int_0^{T/2} (w_t - w_b)\mathrm{d}t, \tag{4.2}$$

where δ_0 is the undisturbed interface thickness and w_t and w_b are the vertical velocities at the top and the bottom of the interface, respectively. Transforming the integral to a spatial integral with $\mathrm{d}x = c\mathrm{d}t$, assuming that $\Delta w = w_t - w_b$ and from $\nabla \cdot \boldsymbol{u} = 0$, we approximate $\Delta w \approx \delta_0 \Delta u/\lambda$, and the relationship becomes

$$\delta_s \approx \delta_0 + \frac{1}{c}\int_0^{\lambda/2} \frac{\delta_0 \Delta u(x)}{\lambda}\mathrm{d}x. \tag{4.3}$$

Assuming $\Delta u(x)$ decays linearly to zero at $x_w = 0.5$, i.e.

$$\Delta u(x) \approx \Delta U(1 - 2x/\lambda), \tag{4.4}$$

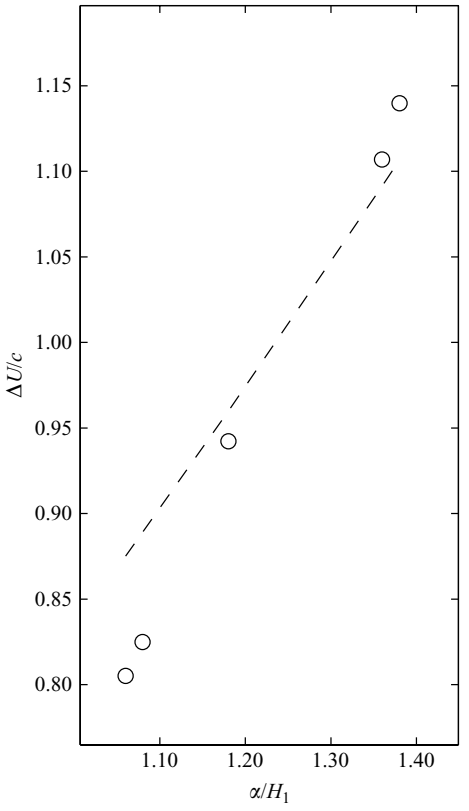

FIGURE 11. Nondimensional wave amplitude versus normalized horizontal velocity difference from simulations (○) and the theoretical approximation from (1.1) (——).

this yields

$$\frac{\delta_s}{\delta_0} \approx 1 + \frac{1}{4}\frac{\Delta U}{c}, \tag{4.5}$$

where ΔU is the horizontal velocity difference between the upper and lower layers at $x_w = 0$ and can be approximated using (1.1). Figure 10(c) shows that $\delta_s/\delta_0 \approx 5/4$, which matches (4.5) for $\Delta U \approx c$ which is the case for these waves. Approximation (1.1) is depicted in figure 11, which shows that the velocity difference can be estimated accurately with the bulk wave parameters, which is also the case for progressive deep interfacial waves as reported by Troy & Koseff (2005). Approximation (1.1) is used in § 5.2, where relationships for the Richardson number are derived as a function of bulk wave parameters.

5. Wave breaking analysis

As was shown by Troy & Koseff (2005), the canonical value of the critical Richardson number of $Ri = 1/4$ is not a sufficient condition for instability and breaking in these waves. This can clearly be seen in the time series of the Richardson numbers depicted in figure 5(b), which indicate that the Richardson number at the trough of the waves is subcritical, although the simulations with $\delta_0/H_1 \geqslant 0.4$ (cases 8F and 16F) are clearly not breaking. An explanation for this behaviour has been provided by Troy & Koseff (2005) who used laboratory experiments to show that progressive interfacial waves are unstable to shear only if the Richardson number

falls below the critical value for long enough periods. In this section the theory of Troy & Koseff (2005) is extended by first employing a detailed stability analysis (§ 5.1). This is followed by the development of an improved method to estimate the minimum Richardson number within a wave based on bulk parameters in § 5.2, which builds upon the work of Bogucki & Garrett (1993).

5.1. *Linear stability analysis*

To determine the nature of the instabilities that develop in our simulations, a perturbation wave amplitude $\alpha' = \alpha - \overline{\alpha}$ is computed, which is a departure of the maximum amplitude of the wave from the low-pass value $\overline{\alpha}$. The low-pass amplitude is obtained through a best-fit linear regression of α in figure 5(a) during the period $17.9 < t/T \leqslant 18.9$ and represents the amplitude history of the wave as it decays roughly linearly in time for this short interval. Although the decay is not strictly linear, the time interval is small enough to eliminate low-frequency bias in the resulting α' signal. Plots of α' are depicted in figures 12(a)–12(e). Recalling that not every case out of cases 1, 2, 4, 8 and 16F exhibits actual breaking through overturning, the series illustrate that they all exhibit physical oscillations in the amplitude time series that may or may not lead to instability. These oscillations originate from numerical errors, both from the stopping tolerance of the elliptic and parabolic solvers and from $O(\Delta x^2)$ spatial and temporal discretization errors. The instabilities are excited by the numerical errors and subsequently grow because of physical mechanisms.

The amplitude oscillations in figure 12 are signatures of perturbations that pass through the trough in a frame of reference that follows the leading wave. The series in figures 12 (a)–12(c) depict spikes followed by regions of smooth decay. These cusped signatures result from the discontinuous nature of the amplitude of the ρ_0 isopycnal located at $x = x_t$, since x_t jumps between local instability troughs. These are not apparent in figures 12 (d)–12(e) because of the lack of billows. A possible time scale that may appear in high-frequency time series of the results is that associated with AMR regridding or the process of addition and removal of various mesh refinement patches as the simulation progresses. Frequent regridding is required so that regions of interest remain at the finest resolution. In the present simulations, regridding occurs every four time steps or roughly every $t/T = 0.004$. Because it is small, the regridding frequency does not show up as a significant component of the signals of α'.

It is possible to assess whether the disturbances are a result of a growing shear instability by determining if the root mean square (r.m.s.) amplitude of the perturbations, $\langle \alpha' \rangle$, is related to that predicted from theory. Following Troy & Koseff (2005), one can assume that if a parcel of fluid at the pycnocline is subject to a subcritical Richardson number for a given period of time, then the amplitude, a_i, of an associated instability will grow exponentially according to

$$\frac{\mathrm{d}a_i}{\mathrm{d}t} = \sigma_i a_i, \tag{5.1}$$

where σ_i is the growth rate of the instability. This equation can be converted to a spatially-varying equation in a wave-following coordinate system with $x_L = (x - ct)/L = x_w \lambda / L$, where c is the wave speed and L is the solitary wave half-width, such that the solitary wave shape can be approximated with $\zeta = \alpha \mathrm{sech}^2(x/L)$. Applying the coordinate transformation to (5.1) and integrating yields

$$\log\left(\frac{a_i}{a_{i_0}}\right) = \overline{\sigma_i} T_w, \tag{5.2}$$

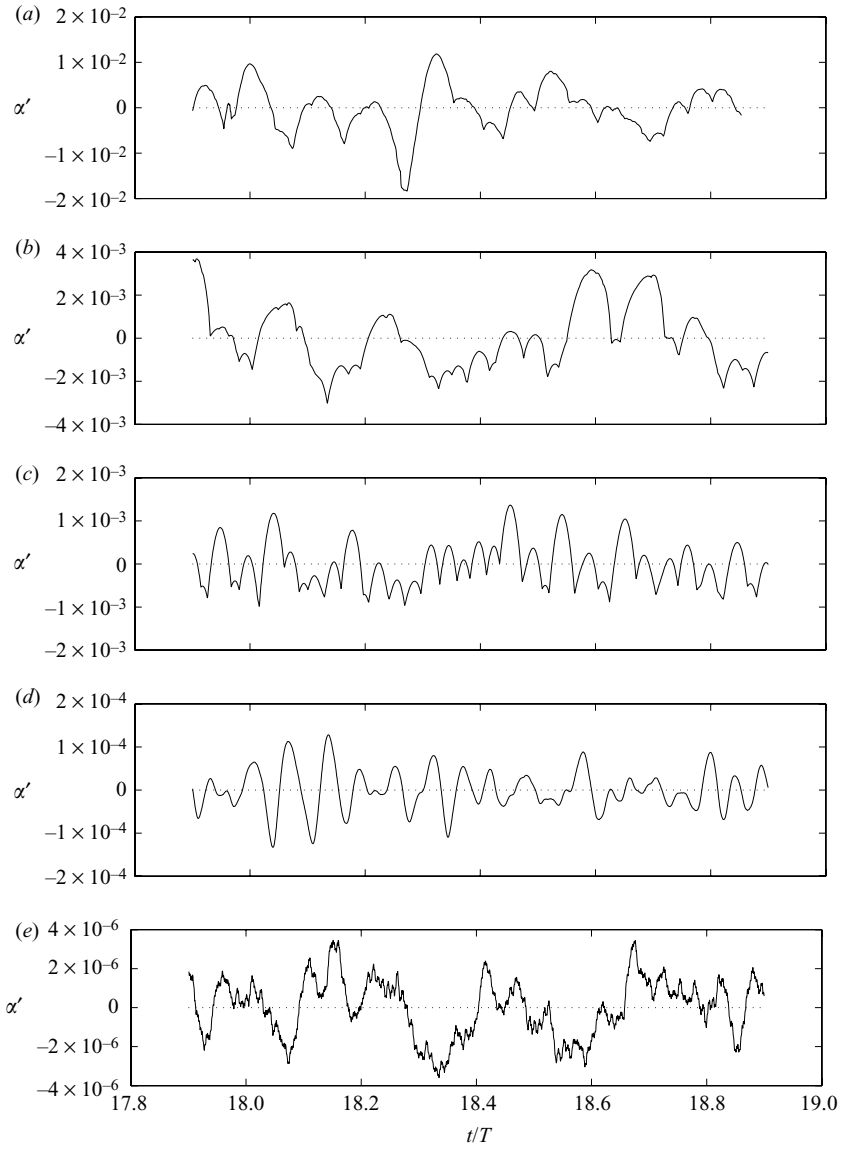

FIGURE 12. Time series of the perturbation amplitude α' for cases (*a*) 1F, (*b*) 2F, (*c*) 4F, (*d*) 8F and (*e*) 16F. Note that the vertical scale is different for each plot.

where a_{i_0} is the initial amplitude of the perturbation, and the average growth rate within the region in which $Ri < 1/4$ upstream of the wave trough is given by

$$\overline{\sigma_i} = \frac{L}{L_w} \int_0^{L_w/L} \overline{\sigma}_i(x_L)\, \mathrm{d}x_L. \tag{5.3}$$

Here, the non-dimensional distance from the trough of the wave to the location in which the local Richardson number falls below 1/4 is L_w/L (L_w is related to the pocket width of possible instability, L_x, by Fructus *et al.* 2009, via $L_x = 2L_w$). The

Case	$\frac{\delta_0}{H_1}$	$\frac{\alpha}{H_1}$	$\frac{\delta_s}{\delta_0}$	$\Delta U/c$	$\log\left(\frac{\langle\alpha'\rangle}{\alpha'_0}\right)$	$\overline{\sigma}_i T_w$	$\overline{\sigma}_{i,e} T_w$	λ_i/δ_0	$Ri_{\min}$	Billows
16F	0.80	1.38	1.28	1.14	0.37	0.35	1.66	2.56	0.213	No
4FSS	0.20	0.95	1.06	0.78	–	2.72	4.19	3.93	0.123	No
8F	0.40	1.36	1.20	1.11	3.75	3.77	4.17	2.88	0.118	No
4FS	0.20	1.15	1.08	0.90	–	5.07	4.81	3.98	0.095	Yes
8FL	0.40	1.43	1.20	1.09	–	5.21	4.93	2.88	0.109	Yes
4F	0.20	1.18	1.29	0.94	6.20	5.38	5.50	4.22	0.085	Yes
8FLL	0.40	1.46	1.20	1.10	–	6.29	5.50	2.88	0.110	Yes
2F	0.10	1.08	1.17	0.83	7.17	–	–	–	0.106	Yes
1F	0.05	1.06	1.79	0.81	8.84	–	–	–	0.093	Yes

TABLE 2. Computed values for all cases in order of increasing instability growth rate based on the Taylor–Goldstein analysis ($\overline{\sigma}_i T_w$). Initial nondimensional interface thickness δ_0/H_1, relative wave amplitude α/H_1, strained interface thickness δ_s/δ_0, total velocity difference $\Delta U/c$, non-dimensional growth rate from the perturbation analysis with (5.4), non-dimensional growth rate from the Taylor–Goldstein analysis $\overline{\sigma}_i T_w$, approximate non-dimensional growth rate from analytical expression (5.11), average wavelength of the most unstable mode normalized by the interface thickness, λ_i/δ_0 and Richardson number at the wave trough (x_t, z_t), $Ri_{\min}$. All data are computed from the simulations at time $t/T = 12$. The last column indicates whether billows formed.

associated wave time scale over which an instability has to grow from the point of incipient instability at $x_L = L_w/L$ to $x_L = 0$ is $T_w = L_w T/\lambda$. We note that the expression for the average growth rate from (5.3) is different from that of Troy & Koseff (2005), who computed the average over all, rather than half, of the pocket width. The two formulations are the same if we assume symmetry about the trough, which is a good approximation, particularly since the instabilities always develop before or at the wave trough. Equation (5.2) can then be used to determine the non-dimensional growth rate from the r.m.s. amplitude of the perturbations at the wave trough with

$$\overline{\sigma_i} T_w = \log\left(\frac{\langle\alpha'\rangle}{\alpha'_0}\right). \tag{5.4}$$

Table 2 lists these values for cases 1F, 2F, 4F, 8F and 16F when an initial perturbation amplitude of $\alpha'_0/H_1 = 5 \times 10^{-8}$ is assumed, and the results for cases 4F, 8F and 16F are depicted in figure 14.

To assess the reliability of the perturbation analysis, we present a linear stability analysis with the Taylor–Goldstein equation (e.g. Hazel 1972) using the computed horizontal velocity and density profiles at 10 points within the region of possible instability ($0 \leqslant x_L \leqslant L_w/L$) at $t/T = 12$. Although cases 1F and 2F did not yield reliable results because billows formed ahead of the wave trough and made it difficult to compute growth rates because of strong variability in the velocity and density profiles, figure 13 depicts peak growth rates within the waves for the other cases, moving from $x_L = L_w/L$ to $x_L = 0$. As expected, although the peak growth rates vary significantly with distance from the wave trough, the associated wavelengths, λ_i (average values for each wave are shown in table 2), of the growing modes vary weakly. This is consistent with the findings in other studies (Hazel 1972; Troy & Koseff 2005), which show weak dependence of the optimal wavenumber for instability on the minimum Richardson number. The results indicate that the region in which the growth rate is non-zero upstream of the trough is confined to less than roughly one

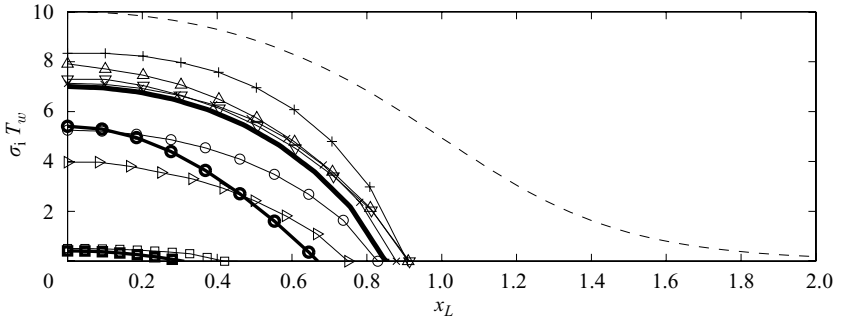

FIGURE 13. Maximum non-dimensional growth rates computed at each location ahead of the wave troughs using the Taylor–Goldstein equation. The dashed line depicts the solitary wave shape from case 8F for reference. The thick solid line depicts a hypothetical wave for which $L_w/L = 0.86$ (from Fructus *et al.* 2009) and $\overline{\sigma}_i T_w = 5$ (from Troy & Koseff 2005). Waves with curves above this case are unstable, while those below it are not. The thick lines with symbols represent approximations using (5.9). Case 16F, □; case 8F, ○; case 4F, △; case 4FSS, ▷; case 4FS, ▽; case 8FL, ×; case 8FLL, +.

quarter of the wave width, and the width of this region increases with increasing peak growth rates which always occur at the wave trough.

Following Troy & Koseff (2005), an estimate for the peak non-dimensional growth rate as a function of x_L is given by

$$\sigma_{i,e}(x_L)T_w = \frac{1}{2}m_0\Delta u(x_L)\left[-0.8Ri(x_L) + 0.2\right], \tag{5.5}$$

where $(1/2)m_0\Delta u(x_L) = \tanh^{-1}(\beta)\Delta u(x_L)/\delta_0$ is an approximation for the vertical shear at the pycnocline and $\Delta u(x_L)$ is the velocity difference across the pycnocline of thickness δ_0. This approximation holds quite well, in particular for use as a guess for the growth rate when solving the Taylor–Goldstein equation. The terms in (5.5) can be approximated analytically rather than computing them at each location with data from the simulations. If the velocity difference across the pycnocline is estimated with

$$\Delta u(x_L) = \Delta U \operatorname{sech}^2(x_L), \tag{5.6}$$

then the Richardson number as a function of x_L can be estimated with

$$Ri(x_L) = \frac{Ri_0}{\operatorname{sech}^4(x_L)}, \tag{5.7}$$

where Ri_0 is the Richardson number at $x_L = 0$ and can be approximated with

$$Ri_0 = \frac{2g'}{m_0\Delta U^2} = \frac{g'\delta_0}{\tanh^{-1}(\beta)\Delta U^2}, \tag{5.8}$$

which differs from the approximation of Bogucki & Garrett (1993) in (1.4) by an amount $1/\tanh^{-1}(\beta)$. Substitution into (5.5) then yields

$$\sigma_{i,e}(x_L)T_w = \frac{1}{2}m_0\Delta U T_w\left(-0.8\frac{Ri_0}{\operatorname{sech}^2 x_L} + 0.2\operatorname{sech}^2 x_L\right). \tag{5.9}$$

The behaviour of this equation is demonstrated in figure 13 for cases 8F and 16F and shows that while the peak growth rate is approximated well, the width of the pocket is underestimated and is probably due to higher-order nonlinear effects not

captured in assuming sech^2 variability for the density and velocity fields. Nevertheless, these errors still enable the approximation to yield reasonable values for the averaged growth rates. Distribution (5.9) can be used to determine the location of incipient instability growth that occurs when $\sigma_{i,e}(x_L)T_w = 0$ or when

$$Ri_0 = \frac{1}{4}\text{sech}^4\left(\frac{L_w}{L}\right). \tag{5.10}$$

Fructus *et al.* (2009) indicated that L_w/L was a better indicator of instability than Ri_0 in breaking interfacial solitary waves, since their results indicated a clearer distinction between breaking and non-breaking waves based on the value of L_w/L rather than Ri_0. Accordingly, they found that waves broke very clearly when $L_w/L > 0.86$, but there was a spread in the breaking values for the minimum Richardson number, which for breaking requires $Ri_0 < 0.1 \pm 0.016$. Employing (5.10) with the condition $L_w/L > 0.86$ implies that $Ri_0 < 0.07$, which, although lower than the lowest value obtained by Fructus *et al.* (2009), is quite close given the number of approximations employed and the simplicity of (5.10).

While Fructus *et al.* (2009) found a threshold for breaking based on the value of L_w/L, Troy & Koseff (2005) found that instability occurred in progressive interfacial waves when $\overline{\sigma}_i T_w > 5$. In terms of a growth time scale, $\tau_i = 2\pi/\sigma_i$, this condition requires that $T_w/\tau_i > 5/2\pi \sim 0.8$, which implies that for instability the instability growth rate must be shorter than 1.25 times the wave time scale. Alternatively, the condition of Troy & Koseff (2005) can be thought of as a spatial restriction on the wavelength of the instabilities if they are to develop in the region in which $Ri < 1/4$. In this case the optimal wavelength of the instability must be smaller than the width of the region in which $Ri < 1/4$ and satisfy $\lambda_i/L_w < (2\pi/5)c_i/c$, where $c_i = 2\pi\sigma_i/\lambda_i$ is the imaginary part of the phase speed associated with the growing instability.

Using the two criteria for instability from Fructus *et al.* (2009) and Troy & Koseff (2005), it is possible to construct a distribution of growth rates that satisfies $L_w/L = 0.86$ and $\overline{\sigma}_i T_w = 5$ by scaling the distribution of growth rates for case 8F. This curve is indicated in figure 13 and falls directly below the curves for the unstable waves and above the curves for the stable waves. To assess whether or not an instability occurs given these growth rate curves, average non-dimensional growth rates are obtained by integration of the growth rates obtained from the Taylor–Goldstein equation using (5.3). These can then be compared with the average non-dimensional growth rate obtained via integration of (5.9), which is given by

$$\overline{\sigma}_{i,e}T_w = \frac{1}{10}m_0\Delta U T_w\left[-4Ri_0\left(1+\frac{1}{2}\frac{L}{L_w}\sinh\left(\frac{2L_w}{L}\right)\right)+\frac{L}{L_w}\tanh\left(\frac{L_w}{L}\right)\right]. \tag{5.11}$$

The average non-dimensional growth rates are depicted in figure 14, which shows that (5.11) approximates the values computed with the Taylor–Goldstein equation quite well. Furthermore, the plot indicates that the perturbation analysis also provides a good measure of the non-dimensional growth rate via (5.4). The three methods all indicate that waves develop instabilities when the non-dimensional growth rate exceeds the critical value of $\overline{\sigma}_c T_w = 5$. This is the same value that was computed by Troy & Koseff (2005) for progressive interfacial waves but is larger than the value of Fructus *et al.* (2009) for solitary waves. Fructus *et al.* (2009) computed non-dimensional growth rates with $F = \gamma L_x/(2|c - c_r|)$, which is related to the non-dimensional growth rates in the present study via $F = \alpha_{avg}\overline{\sigma}_i T_w/|1 - c_r/c|$, where c_r is the propagation speed of the most unstable modes and the factor $\alpha_{avg} = \max(\sigma_i)/\overline{\sigma}_i$

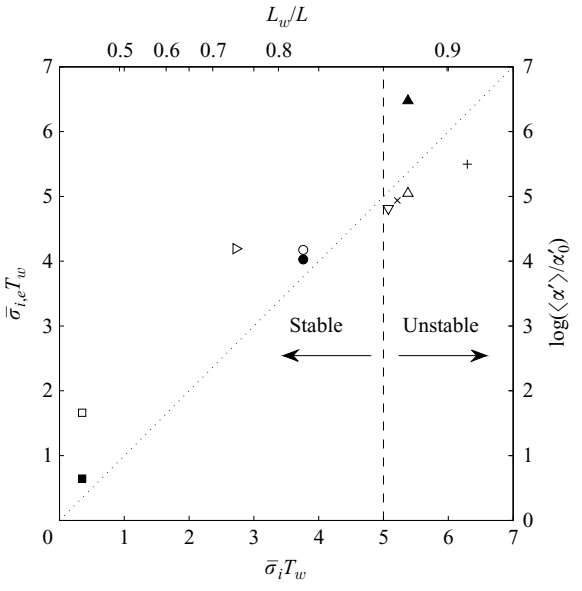

FIGURE 14. Comparison of the non-dimensional average growth rates computed with the Taylor–Goldstein equation, $\overline{\sigma}_i T_w$, with those approximated using (5.11) to obtain $\overline{\sigma}_{i,e} T_w$: Case 16F, □; case 8F, ○; case 4F, △; case 4FSS, ▷; case 4FS, ▽; case 8FL, ×; case 8FLL, +. Growth rates computed from the perturbation analysis with (5.4) are also shown, denoted by filled symbols. The vertical dashed line corresponds to the breaking thresholds of Troy & Koseff (2005) and Fructus *et al.* (2009), which imply breaking for $\overline{\sigma}_i T_w > 5$ or, equivalently, $L_w/L > 0.86$, as indicated by the top x-axis label.

accounts for the fact that the average growth rate is smaller than the maximum growth rate by, on average for the present simulations, $\alpha_{avg} = 1.4$. The minimum non-dimensional growth rate in Fructus *et al.* (2009) for the breaking waves was 0.9, while the maximum non-dimensional growth rate for the stable waves was 1.16, indicating that the breaking threshold for their waves was roughly $\overline{\sigma}_i T_w > 1$. We hypothesize that the smaller threshold may be due to the disturbances present in the laboratory experiments that may lead to instability for a lower threshold than in the present simulations, which develop out of perturbations associated with small errors in the numerical method. Furthermore, they employ linear stratifications in their pycnocline (at least as close to one as they could get in laboratory experiments). This could also contribute to differences in the breaking threshold. Nevertheless, the perturbations in the laboratory experiments indicate that the threshold value obtained in the present simulations is probably an upper bound relative to what may happen in the field, where the threshold is probably much smaller because of the presence of perturbations associated with background turbulence.

The equality of the breaking threshold for the progressive waves of Troy & Koseff (2005) and the solitary waves in the present study probably results because the horizontal wavelength of the most unstable modes in the present study and that of Troy & Koseff (2005) is much smaller than the horizontal scale of the waves (from table 2, $\lambda_i/\lambda < 0.08$). The weak spatial variability, and hence weak temporal variability of the flow relative to that of the instabilities, justifies use of the Taylor–Goldstein equation to compute the local growth rates of the instabilities within the pocket of potential instability. Effectively, the instability in the present study and

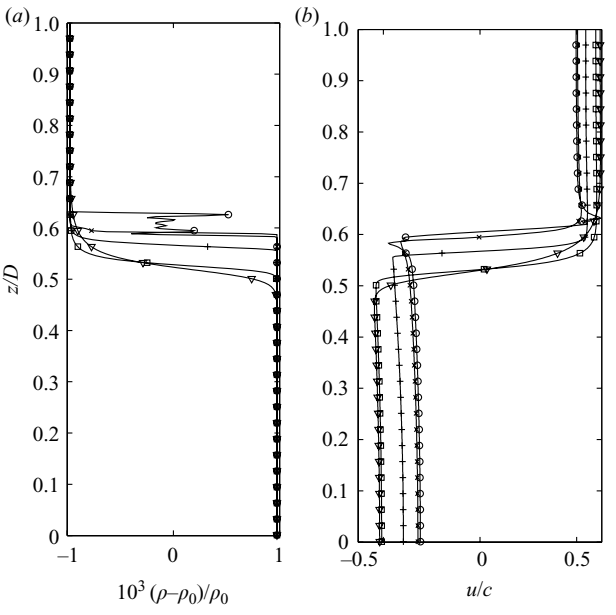

FIGURE 15. Normalized vertical profiles of (*a*) density and (*b*) horizontal velocity at $t/T = 12$ and at $x_w = 0$. The symbols indicate cases 1F (○), 2F (×), 4F (+), 8F (□) and 16F (▽).

that of Troy & Koseff (2005) is a modified shear instability in a stratified shear flow that is well approximated with hyperbolic tangent density and velocity profiles that vary weakly in the horizontal and slowly in time. Although validity of the Taylor–Goldstein equation enables its use for determination of threshold values for $\overline{\sigma}_i T_w$ and L_w/L, these are not as practical for determination of instability in the ocean because they require knowledge of the spatial distribution of growth rates. Instead, a more reasonable method of assessing instability is based on the value of the minimum Richardson number within the wave, which we discuss in the next section.

5.2. *Critical Richardson number based on bulk wave parameters*

When Bogucki & Garrett (1993) derived the critical breaking amplitude for solitary-like interfacial waves, the result was approximate for two reasons, the first of which is assumption of the canonical Richardson number of 1/4 which is too large, and the second of which is due to errors in the approximation for Ri in (1.4). These errors arise mostly because it is difficult to determine the actual minimum Richardson number within a wave based on the bulk wave parameters because of the nonlinear behaviour of the shear and stratification profiles and simply because it is always not clear how to define the actual thickness of the pycnocline, as demonstrated by the profiles depicted in figure 15. In what follows, we refer to the approximation in (1.4) as method BG which, when compared to the minimum Richardson number, $Ri_{\min}$, in the waves in the present study is an overestimate. However, method BG can be adjusted by a constant to yield method BGC such that $Ri_{BGC} = \gamma_c Ri_{BG}$, where $\gamma_c = 0.62$ is obtained through a least squares linear fit between the values of Ri_{BGC} and $Ri_{\min}$ for the non-breaking simulations (cases 4FSS, 8F, 16F). The results are depicted in figure 16, which shows that the approximation Ri_{BGC} closely follows the values of $Ri_{\min}$. When billows form, however, method BGC underestimates the minimum Richardson number for the breaking cases because the computed solution

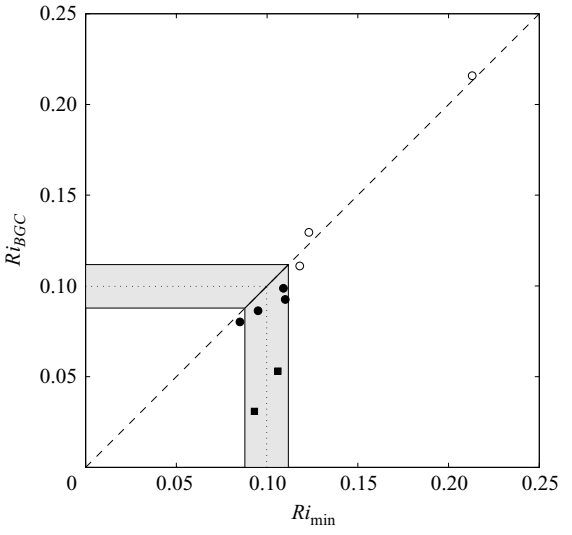

FIGURE 16. Comparison of the estimate for the minimum Richardson number based on the corrected value of Bogucki & Garrett (1993), Ri_{BGC}, with the minimum value computed in the present simulations, $Ri_{\min}$. The open circles are stable waves, while the closed circles are unstable waves, and the filled squares are unstable waves with billows that degrade the accuracy of Ri_{BGC}. The shaded region corresponds to $Ri_c = 0.1 \pm 0.01$. Note that axes maxima are given by the canonical Richardson number of 1/4.

contains billows that have formed and lead to interface thickening and a reduction in the vertical shear which causes $Ri_{\min}$ to increase. The severest cases in figure 16 (indicated by the squares in the figure for cases 1F and 2F) contain strong billows which effectively inhibit the minimum Richardson number. This critical value can be estimated by taking the average minimum Richardson number for all breaking cases to be $Ri_c = 0.1 \pm 0.01$, which is indicated by the shaded region in figure 16 and is within the ranges predicted in other studies, i.e. $Ri_c = 0.075 \pm 0.035$ (Troy & Koseff 2005) and $Ri_c = 0.092 \pm 0.016$ (Fructus *et al.* 2009).

Based on the bulk parameters, the simulation results indicate that a sufficient criterion for instability in internal solitary-like waves is given by

$$0.62 Ri_{BG} = Ri_{BGC} < 0.1 \pm 0.01. \tag{5.12}$$

This can be interpreted either as a modified threshold for the approximations of Bogucki & Garrett (1993), such that $Ri_{BG} < 0.16 \pm 0.02$, or as a modification of the estimate Ri_{BG} to obtain Ri_{BGC} given a critical Richardson number of $Ri_c = 0.1 \pm 0.01$. Modification of Ri_{BG} can be interpreted as approximating the Richardson number using a modified interface thickness $\delta' = 0.62\delta_0$, which represents a more accurate estimate of the vertical gradients in the velocity and density fields. From figure 15 it is clear that the maximum vertical derivatives are greater than simple estimates based on $\rho_z = \Delta\rho/\delta_0$ and $u_z = \Delta U/\delta_0$. Insight into the effects of the vertical profiles on the estimate of Ri can be obtained through analysis of idealized profiles of $\rho(z)$ and $u(z)$ of the form

$$\rho(z) = \rho_0 - \frac{\Delta\rho}{2}\tanh(m_\rho z), \tag{5.13}$$

$$u(z) = \frac{\Delta U}{2}\tanh(m_u z), \tag{5.14}$$

where

$$m_\rho = \frac{2\tanh^{-1}(\beta)}{\delta_\rho}, \tag{5.15}$$

$$m_u = \frac{2\tanh^{-1}(\beta)}{\delta_u}, \tag{5.16}$$

and where δ_ρ and δ_u are the effective thicknesses of the pycnocline and shear layer, respectively. These profiles imply

$$\rho(z = +\delta_\rho/2) - \rho(z = -\delta_\rho/2) = -\beta\Delta\rho, \tag{5.17}$$

$$u(z = +\delta_u/2) - \rho(z = -\delta_u/2) = \beta\Delta U, \tag{5.18}$$

so that the vertical derivatives at $z = 0$ are given by

$$\frac{\partial\rho}{\partial z} = -\frac{1}{2}m_\rho\Delta\rho,$$

$$\frac{\partial u}{\partial z} = \frac{1}{2}m_u\Delta U,$$

and the Richardson number at $z = 0$ is given by

$$Ri = \frac{1}{\tanh^{-1}(\beta)}\left(\frac{\delta_u}{\delta_\rho}\right)\frac{g'\delta_u}{\Delta U^2}, \tag{5.19}$$

which differs from the approximation for Ri_{BG} by the constant $\delta_u^2/(\delta_0\delta_\rho\tanh^{-1}(\beta))$. If $\delta_u = \delta_\rho = \delta_0$, then the approximation for Ri_{BG} reverts to Ri_{BGC} if an effective interface thickness of $\delta_0/\tanh^{-1}(\beta)$ is used with $\beta = 0.925$, since $1/\tanh^{-1}(0.925) = 0.62$. Although the velocity and density profiles in solitary-like interfacial gravity waves are given only approximately by hyperbolic tangent distributions, this analysis highlights how the approximation Ri_{BG} can be improved through derivation of a constant that requires assumptions about the velocity and density fields beyond linear distributions in the vertical coordinate.

With improved estimates for Ri and a sufficient condition for instability that requires $Ri < 0.1$, the critical amplitude for instability as a function of the non-dimensional interface thickness δ_0/H_1 is presented in figure 17. Method BG is used to predict the critical steepness by assuming the canonical value of $Ri = 1/4$, as was done by Bogucki & Garrett (1993), while method BGC is used to predict the critical amplitude using the critical Richardson number of 0.1 obtained in the present paper (5.12). The relationship derived by Troy & Koseff (2005), $(\alpha_c/H_1)^2 = \delta_0/H1/(5.3Ri_c kH_1)$, with $Ri_c = 0.075$, is also included for comparison. The results indicate that (5.12) (method BGC with $Ri_c = 0.1$) is the most reliable predictor of the critical amplitude leading to instability for the parameter space employed in this paper. Use of method BG along with the canonical value for the critical Richardson number would imply that cases 8F and 4FSS should be unstable, but it is evident that $Ri = 1/4$ is not a sufficient condition for instability, since these cases do not exhibit billows of the Kelvin–Helmholtz type.

In an effort to limit the parameter space employed in this study, we ignored the effects of varying the depths of the upper and lower layers, H_1 and H_2, or simply the parameter H_1/H_2, by keeping $H_1/H_2 = 0.25$ fixed. The effects of H_1/H_2 are depicted in figure 18, which uses the BGC estimate for Ri and shows contours of $Ri = Ri_c = 0.1$ in the α/H_1–H_1/H_2 plane for different values of δ_0/H_1. The figure enables evaluation of the critical amplitude for breaking as the point in which the $Ri = Ri_c$ contours

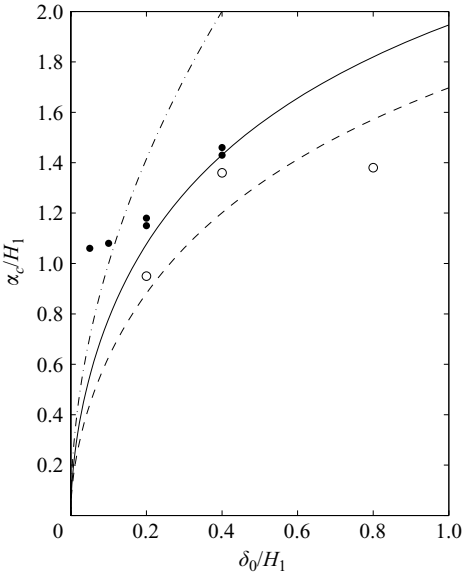

FIGURE 17. Non-dimensional critical breaking amplitude as computed using three different approximations: method BG with $Ri_c = 1/4$ (dashed line), method BGC with $Ri_c = 0.1$ (solid line) and the approximation of Troy & Koseff (2005) with $Ri_c = 0.075$ (dash-dotted line). Simulation results that exhibit breaking are represented by the filled circles, while those that do not are represented by the open circles.

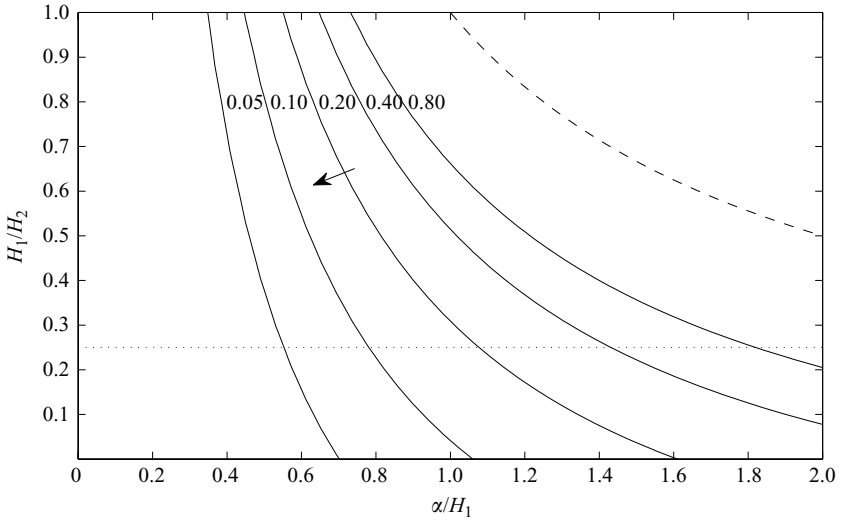

FIGURE 18. Contours of $Ri = Ri_c$ in the α/H_1–H_1/H_2 plane for different values of δ_0/H_1. The dotted line depicts the case for the present study, $H_1/H_2 = 0.25$. The dashed line is the solitary wave amplitude limit for a two-layer stratification, where the maximum amplitude is H_2. Waves are stable to the left of the contours, as indicated by the arrow.

intersect a line of constant H_1/H_2. For example, the critical breaking amplitudes for each δ_0/H_1 in the present study are indicated by the points at which the $Ri = Ri_c$ contours intersect the dashed line representing $H_1/H_2 = 0.25$. For fixed δ_0/H_1 and H_1/H_2, increasing the amplitude can lead to instability because of a reduction in the Richardson number. At the same time, for fixed δ_0/H_1 and α/H_1, increasing the depth

of the upper layer thickness H_1 relative to the lower layer thickness H_2 can also lead to instability. The sensitivity of the breaking amplitude to the layer depths is weak for small δ_0/H_1, while it is stronger for larger δ_0/H_1. This behaviour is indicated by the slope of the $Ri = Ri_c$ contours, which decreases in absolute value as δ_0/H_1 increases, particularly for small values of H_1/H_2. Future studies could verify the sensitivity of the instability to changes in H_1/H_2, and we suspect this will not change the critical value of $Ri_c = 0.1$ given that a similar value has been observed in other independent studies (Fringer & Street 2003; Troy & Koseff 2005; Fructus *et al.* 2009).

6. Comparison to observations

The qualitative features of the formation of small-scale Kelvin–Helmholtz billows as depicted in figure 4 are similar to those in the wave in figure 5 of Moum *et al.* (2003), which depicts a solitary wave with undisturbed stratification ahead of it and instabilities that form at its trough and persist in the wake of the wave. The zoomed-in view in figure 4 of the current paper depicts what high-resolution backscatter imagery of field observations would likely reveal, in that, as hypothesized by Moum *et al.* (2003), billows of the Kelvin–Helmholtz type form at the wave trough and lead to enhanced mixing and dissipation along the pycnocline downstream. However, because the observed stratification is much more complex than the stratification employed in the present paper, in that it consists of several density steps, it is difficult to make direct comparisons with our simulations. We hypothesize this to be the reason why our simulations do not reveal any pronounced billows of the Kelvin–Helmholtz type as shown in figure 14 of Moum *et al.* (2003), which reflect a rarely observed phenomenon (J. Moum 2009, personal communication) that depends on how a particular solitary wave interacts with the local stratification, which itself may be a result of the passage of numerous solitary waves.

7. Three-dimensional effects: primary and secondary instabilities

To demonstrate that the two-dimensional approach is valid for investigating the primary instability mechanism that leads to overturns and breaking, a three-dimensional simulation was conducted to show that the instabilities are primarily two-dimensional. For the three-dimensional simulation the initial conditions are identical to those for case 4C but with an effective resolution of $16\,384 \times 128 \times 256$ (see case 4C3D in table 1). Without AMR this would result in over 536 million grid cells, but with AMR the number of cells is reduced by roughly one order of magnitude, and the calculation is tractable using 1024 processors for three weeks on a parallel machine. This represents a computational effort of roughly 5 00 000 processor hours or 60 processor years. The three-dimensional discretization yields $\Delta x = 0.6$ m, $\Delta y = 0.6$ m, $\Delta z = 0.4$ m for a 10 km long, 78.25 m wide and 100 m deep domain. This resolution, for a field-scale flow, is unprecedented in numerical simulations of environmental flows.

Periodic boundary conditions are imposed in the lateral (y) dimension. To trigger possible three-dimensional instabilities the initial interface is perturbed as follows:

$$\psi(x, y, t = 0) = H_2 - \alpha_0 \exp\left(-\frac{x^2}{\sigma^2}\right) + r(x, y), \tag{7.1}$$

where $-0.005\delta_0 < r(x, y) < 0.005\delta_0$ is a uniformly-distributed random number. In figure 19 a sequence of progressively zoomed-in isosurfaces of ρ_0 coloured by the lateral velocity is shown, where red is positive and blue is negative. The figure

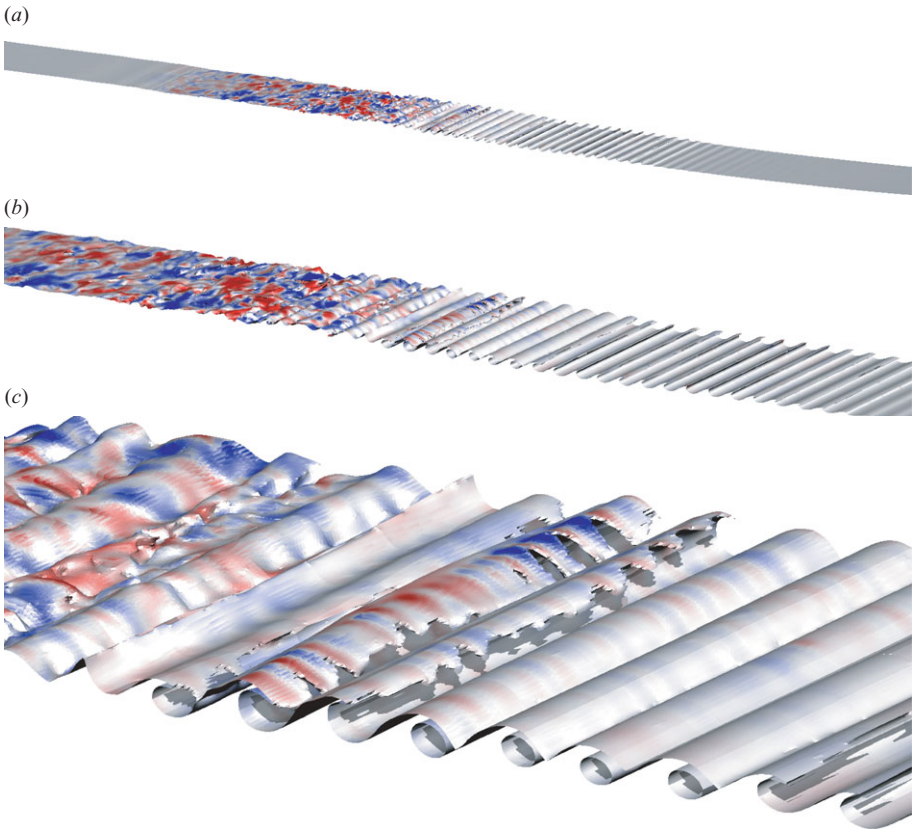

FIGURE 19. A three-dimensional simulation for case 4C3D, at $t/T = 2.4$. The density isosurface is of the ρ_0 isopycnal, and the colour indicates lateral velocity (red is positive lateral velocity and blue negative lateral velocity). In (*a*), the nearly solitary wave is truncated on the right side, and the trough is roughly where the instabilities become visible. In (*c*), the lateral disturbances are of the order of the billow diameter (which can be measured in figure 20).

demonstrates that the incipient instability is a two-dimensional instability, followed by three-dimensional lateral instabilities, much like those found by Fringer & Street (2003). It is likely that the waves are not susceptible to an incipient three-dimensional instability, such as that found by Smyth & Peltier (1990), because the initial three-dimensional instability in that work occurred for low Reynolds numbers ($Re < 300$), while in the present simulations $Re \gg 300$. The two-dimensional and then the three-dimensional instability sequence that we observe is in agreement with that of Squire (1933), in whose work it was shown that for parallel shear flows, two-dimensional instability growth rates are larger than three-dimensional instability growth rates. This can be seen by scanning from right to left in figure 19(*b*).

To further verify that three-dimensional effects do not alter the behaviour of the incipient two-dimensional instability, figure 20 presents a comparison between the two-dimensional and three-dimensional simulations at $t/T = 1.5$. The initial instability occurs at the same location in both simulations, although the amplitude of the isopycnal displacements in the two-dimensional simulation is slightly larger. This is as expected, since three-dimensional lateral instabilities quickly lead to dissipation that reduces the lateral vorticity magnitude of the overturning billows. This dissipation also leads to a slightly slower and smaller wave in the three-dimensional case, which causes

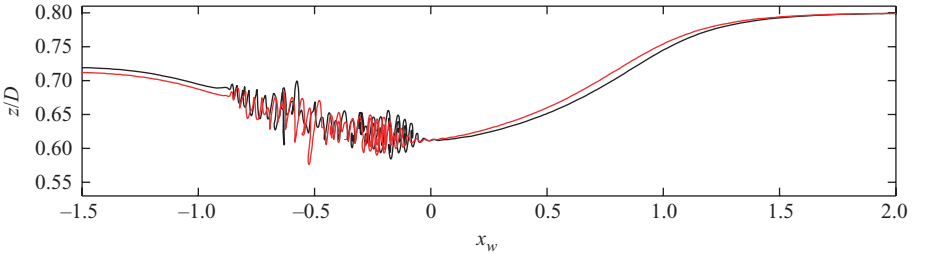

FIGURE 20. Comparison of the ρ_0 isopycnal for the two-dimensional (black) and three-dimensional (red) simulations at time $t/T = 1.5$. The resolution in the x and z directions for these two simulations is identical (cases 4C and 4C3D).

the two-dimensional wave to slightly lead the three-dimensional wave in the figure. The slight discrepancy in the wave amplitude (α) between the two is also a source of a weaker incipient two-dimensional instability for the three-dimensional run. While this reduces the amplitude of the incipient billows for the three-dimensional run, it is suspected that most of the reduction in amplitude of the overturning billows that is evident in the figure is due to dissipation resulting from three-dimensional lateral instabilities. These dynamics do not affect the incipient instability which is primarily two-dimensional and independent of the mixing and dissipation, a discussion of which we leave to a future work on three-dimensional dynamics and energetics.

8. Conclusions

While ubiquitous, shear instabilities in open-ocean internal solitary-like waves are rarely observed because the size of the associated billows of the Kelvin–Helmholtz type is beyond the resolution of typical echosounder data. Numerical simulation of these instabilities is equally difficult because of the resolution required to resolve the large range of scales involved. We have shown that the problem is tractable with AMR because of the ability to refine only where high resolution is needed, thereby enabling simulation that resolves billows that are roughly 5 m in diameter that form within waves that are roughly 500 m long in a domain that is 10 km long. Our simulations compare well in a qualitative sense with those of Moum *et al.* (2003), although the simulations do not exhibit the observed large-scale billows that are of the order of the amplitude of the waves upon which they form. These large-scale billows are probably rare, and most billows that form at the interface in solitary-like waves behave much like those in our simulations. However, because the open-ocean environment in which solitary-like waves propagate is far from quiescent, billow formation in solitary-like waves in natural waters probably occurs under less restrictive criteria than we have derived in this paper, since the solitary-like waves in our simulations propagate into a quiescent fluid. Therefore, we note that although the length scales in this paper are representative of real open-ocean solitary-like waves, the stability criteria are representative of idealized settings.

Using the AMR technique, two-dimensional simulations were conducted over a parameter space that held the depth of the pycnocline constant and focused on the influence of the interface thickness and wave amplitude on the development of a shear instability. The interface thickness affected the amplitude of the waves that we studied because of the formation of shear instabilities and associated dissipation as the leading solitary-like waves emerged from the initial Gaussian of depression. As a result, waves

with thinner interfaces emerged from the wave trains with smaller amplitudes, and the subsequent amplitude decay was stronger in the presence of billows. Nevertheless, the waves that emerged formed a set of waves in which instability could be analysed as a function of wave amplitude and interface thickness. It was shown that vertical strain at the interface was always positive, leading to thickening of the interface at the wave trough that, coupled with an increase in the vertical shear, led to a pronounced drop in the Richardson number that was always a minimum at the wave troughs. All of the minimum Richardson number values in the nine waves that were studied were below the canonical value of 0.25, the largest of which was 0.213 (case 16F) and the smallest of which was 0.085 (case 4F). However, three of the cases did not lead to the formation of billows. For waves that exhibited overturning, billows formed in the wave trough, and a three-dimensional simulation showed that the initial instability is two-dimensional, while subsequent billow breakdown is three-dimensional. Waves with a particular interface thickness that did not exhibit overturning could be made to exhibit billows by increasing the wave amplitude. In particular, case 8F was stable, but instability occurred when its amplitude was 5 % larger, as in case 8FL. Likewise, case 4FS was unstable, but decreasing its amplitude by 17 % led to stability, as exhibited by case 4FSS. One could imagine this situation in the field in which solitary-like wave amplitude changes may result from the presence of topography or lateral variability in the stratification.

Although all waves did not exhibit billows of the Kelvin–Helmholtz type, all waves did exhibit oscillations of isopycnals at the wave trough. Because of the presence of destabilizing shear in the waves, growth rates as computed by the Taylor–Goldstein equation along different locations upstream of the wave trough where $Ri < 1/4$ were always positive. However, unless the instabilities had time to grow and manifest themselves as billows, they were simply advected past the wave trough (in a frame moving with the waves) and appeared as perturbations in the isopycnal displacements. It was shown that the amplitude of these oscillations compared favourably with those predicted with an analysis of the instabilities with the Taylor–Goldstein equation. Using the Taylor–Goldstein equation with vertical velocity and density profiles at different locations upstream of the wave troughs, the distribution of growth rates within the waves could be determined. The distance from the wave trough to the point upstream of the trough at which the growth rate first became positive (which occurs when $Ri < 1/4$) was defined by L_w, and we found that waves that exhibited instability all had $L_w/L > 0.86$, where L is the wave half-width. This value agrees with that of Fructus *et al.* (2009), who noted that L_w/L, or the non-dimensional width of the 'pocket' of instability, was a more precise indicator of instability than the minimum Richardson number. Calculating an average growth rate of the instabilities within the pocket of instability showed that instability also occurred when $\overline{\sigma}_i T_w > 5$, where $\overline{\sigma}_i$ is the average growth rate and T_w is the time in which fluid parcels are subjected to $Ri < 1/4$. This condition agrees with that of Troy & Koseff (2005) and implies that the time scale of the instability must be less than 1.25 times the time scale in which it is subjected to destabilizing shear in order for billows to form.

While the criteria for instability based on L_w/L or $\overline{\sigma}_i T_w$ are sufficient, a more attractive criterion is based on the minimum Richardson number within the wave because instability can be assessed via a pointwise value of Ri rather than via quantities that require information about the distribution of Ri within the wave. Our simulations show that a sufficient criterion for instability requires the minimum Richardson number within a wave to fall below $Ri_c = 0.1 \pm 0.01$ and is consistent with the findings in other studies. After employing a correction derived from use of an

effective interface thickness, the approximation of Bogucki & Garrett (1993) provides for a convenient way to determine stability properties of solitary-like interfacial gravity waves based on bulk wave parameters. The approximation can then be used to assess the critical amplitude for instability given H_1/H_2 and δ_0/H_1. Although our study assumed H_1/H_2 constant, we hypothesize that because the critical Richardson number required for instability falls within the range of other studies, one of which employed infinitely deep fluids (Troy & Koseff 2005) and the other of which studied a wide range of H_1/H_2 (Fructus *et al.* 2009), the minimum Richardson number required for instability should not be a strong function of H_1/H_2. Whether or not a universal critical Richardson number exists that forms a sufficient criteria for instability in all unsteady stratified shear flows, of course, remains to be seen.

We thank Jim Moum for discussions regarding his observations of billows in internal solitary-like waves, Cary Troy for numerous discussions and for providing his Matlab code and advice with the Taylor–Goldstein analysis, Phil Colella and his staff at LBNL for collaborative support and three anonymous referees whose comments helped improve the quality of the paper. MFB acknowledges the support of the NSF MSPRF programme. MFB and OBF acknowledge the support of ONR grant N00014-05-1-0294 (scientific officers Dr C. Linwood Vincent, Dr Terri Paluszkiewicz and Dr Scott Harper). We are grateful for the access to computational resources from the Center for Computational Earth and Environmental Sciences at Stanford University, the ARL Major Shared Resource Center as part of a DOD Challenge Allocation and the National Energy Research Scientific Computing Center, which is supported by the Office of Science of the US Department of Energy under contract no. DE-AC02-05CH11231.

REFERENCES

Almgren, A. S., Bell, J. B., Colella, P., Howell, L. H. & Welcome, M. L. 1998 A conservative adaptive projection method for the variable density incompressible Navier–Stokes equations. *J. Comput. Phys.* **142**, 1–46.

Armi, L. & Farmer, D. M. 1988 The flow of mediterranean water through the Strait of Gibraltar. *Prog. Oceanogr.* **21** (1), 1.

Barad, M. F. & Colella, P. 2005 A fourth-order accurate adaptive mesh refinement method for Poisson's equation. *J. Comput. Phys.* **209** (1), 1–18.

Barad, M. F., Colella, P. & Schladow, S. G. 2009 An adaptive cut-cell method for environmental fluid mechanics. *Intl J. Numer. Meth. Fluids* **60** (5), 473–514.

Barad, M. F. & Fringer, O. B. 2007 Numerical simulations of shear instabilities in open-ocean internal gravity waves. In *Proceedings of the Fifth International Symposium on Environmental Hydraulics*, Perth, 722–72.

Bell, J., Berger, M., Saltzman, J. & Welcome, M. 1994 Three-dimensional adaptive mesh refinement for hyperbolic conservation laws. *SIAM J. Sci. Comput.* **15** (1), 127–138.

Bell, J. B., Colella, P. & Glaz, H. M. 1989 A second-order projection method for the incompressible Navier–Stokes equations. *J. Comput. Phys.* **85**, 257–283.

Bell, J. B., Day, M. S., Shepherd, I. G., Johnson, M. R., Cheng, R. K., Grcar, J. F., Beckner, V. E. & Lijewski, M. J. 2005 From the cover: numerical simulation of a laboratory-scale turbulent V-flame. *Proc. Natl Acad. Sci.* **102** (29), 10006–10011.

Berger, M. J. & Colella, P. 1989 Local adaptive mesh refinement for shock hydrodynamics. *J. Comput. Phys.* **82** (1), 64–84.

Berger, M. J. & Leveque, R. J. 1989 An adaptive Cartesian mesh algorithm for the euler equations in arbitrary geometries. *AIAA Paper* 89-1930CP. AIAA, pp. 1–7.

Berger, M. J. & Oliger, J. E. 1983 Adaptive mesh refinement for hyperbolic partial differential equations. *Tech Rep*. NA-M-83-02 Stanford University.

Bogucki, D. & Garrett, C. 1993 A simple model for the shear induced decay of an internal solitary wave. *J. Phys. Oceanogr.* **23** (8), 1767–1776.

Cacchione, D. & Wunsch, C. 1974 Experimental study of internal waves over a slope. *J. Fluid Mech.* **66**, 223–239.

Carter, G. S., Gregg, M. C. & Lien, R. C. 2005 Internal waves, solitary-like waves, and mixing on the Monterey Bay shelf. *Cont. Shelf Res.* **25** (12–13), 1499–1520.

Caulfield, C. P. & Peltier, W. R. 2000 The anatomy of the mixing transition in homogeneous and stratified free shear layers. *J. Fluid Mech.* **413**, 1–47.

Diamessis, P. J. & Redekopp, L. G. 2006 Numerical investigation of solitary internal wave-induced global instability in shallow water benthic boundary layers. *J. Phys. Oceanogr.* **36**, 784–812.

Egbert, G. D. & Ray, R. D. 2000 Significant dissipation of tidal energy in the deep ocean inferred from satellite altimeter data. *Nature* **405**, 775–778.

Fjortoft, R. 1950 Application of integral theorems in deriving criteria of stability of laminar flow and for the baroclinic circular vortex. *Geofys. Publ.* **17**, 1–52.

Fringer, O. B. & Street, R. L. 2003 The dynamics of breaking progressive interfacial waves. *J. Fluid Mech.* **494**, 319–353.

Fructus, D., Carr, M., Grue, J., Jensen, A. & Davies, P. A. 2009 Shear induced breaking of large internal solitary waves. *J. Fluid Mech.* **620**, 1–29.

Fructus, D. & Grue, J. 2004 Fully nonlinear solitary waves in a layered stratified fluid. *J. Fluid Mech.* **505**, 323–347.

Gossard, E. E. 1990 *Radar in Meteorology* (ed. D. Atlas), pp. 477–527. American Meteorological Society.

Grue, J., Jensen, A., Rusas, P. O. & Sveen, J. K. 2000 Breaking and broadening of internal solitary waves. *J. Fluid Mech.* **413**, 181–217.

Haigh, S. P. 1995 Non-symmetric Holmboe waves. PhD thesis, University of British Columbia, Vancouver, BC, Canada.

Hazel 1972 Numerical studies of the stability of inviscid stratified shear flows. *J. Fluid Mech.* **51**, 39–61.

Helfrich, K. R. & Melville, W. K. 1986 On long nonlinear internal waves over slope-shelf topography. *J. Fluid Mech.* **167**, 285–308.

Helfrich, K. R. & Melville, W. K. 2006 Long nonlinear internal waves. *Annu. Rev. Fluid Mech.* **38**, 395–425.

Hogg, A. M. & Ivey, G. N. 2003 The Kelvin–Helmholtz to Holmboe instability transition in stratified exchange flows. *J. Fluid Mech.* **477**, 339–362.

Hosegood, P., Bonnin, J. & van Haren, H. 2004 Solibore-induced sediment resuspension in the Faeroe–Shetland channel. *Geophys. Res. Lett.* **31** (9), L09301.

Howard, L. N. 1961 Note on a paper of John W. Miles. *J. Fluid Mech.* **10**, 509–512.

Ivey, G. N. & Nokes, R. I. 1989 Vertical mixing due to the breaking of critical internal waves on sloping boundaries. *J. Fluid Mech.* **204**, 479–500.

Ivey, G. N., Winters, K. B. & Silva, I. P. D. De 2000 Turbulent mixing in a sloping benthic boundary layer energized by internal waves. *J. Fluid Mech.* **418**, 59–76.

Javam, A., Imberger, J. & Armfield, S. W. 1999 Numerical study of internal wave reflection from sloping boundaries. *J. Fluid Mech.* **396**, 183–201.

Klymak, J. M. & Moum, J. N. 2003 Internal solitary waves of elevation advancing on a shoaling shelf. *Geophys. Res. Lett.* **30** (20), 2045.

Kundu, P. K. 2002 *Fluid Mechanics*, 2nd edn. Academic.

Lamb, K. G. 2002 A numerical investigation of solitary internal waves with trapped cores formed via shoaling. *J. Fluid Mech.* **451**, 109–144.

Lamb, K. G. 2003 Shoaling solitary internal waves: on a criterion for the formation of waves with trapped cores. *J. Fluid Mech.* **478**, 81–100.

Legg, S. & Adcroft, A. 2003 Internal wave breaking at concave and convex continental slopes. *J. Phys. Oceanogr.* **33**, 2224–2246.

Long, R. R. 1956 Solitary waves in one- and two-fluid systems. *Tellus* **8**, 460–471.

Marmorino, G. O. 1990 'Turbulent mixing' in a salt finger staircase. *J. Geophys. Res.* **95**, 12983–12994.

Maslowe, S. A. & Redekopp, L. G. 1980 Long nonlinear waves in stratified shear flows. *J. Fluid Mech.* **101**, 321–348.

Michallet, H. & Ivey, G. N. 1999 Experiments on mixing due to internal solitary waves breaking on uniform slopes. *J. Geophys. Res.* **104**, 13 467–13 477.

Miles, J. W. 1963 On the stability of heterogeneous shear flows. Part 2. *J. Fluid Mech.* **16**, 209–227.

Moum, J. N., Farmer, D. M., Smyth, W. D., Armi, L. & Vagle, S. 2003 Structure and generation of turbulence at interfaces strained by internal solitary waves propagating shoreward over the continental shelf. *J. Phys. Oceanogr.* **33**, 2093–2112.

Munk, W. & Wunsch, C. 1998 Abyssal recipes. Part II. Energetics of tidal and wind mixing. *Deep-Sea Res.* **45**, 1977–2010.

Pereira, N. R. & Redekopp, L. G. 1980 Radiation damping of long, finite amplitude internal waves. *Phys. Fluids* **23**, 2182–2183.

Phillips, O. M. 1977 *The Dynamics of the Upper Ocean*. Cambridge University Press.

Rayleigh, J. W. S. 1880 On the stability or instability of certain fluid motions. *Proc. Lond. Math. Soc.* **9**, 57–70.

Scotti, A. & Pineda, J. 2004 Observations of very large and steep internal waves of elevation near the Massachusetts coast. *Geophys. Res. Lett.* **31**, l22307.

Skamarock, W., Oliger, J. & Street, R. L. 1989 Adaptive grid refinement for numerical weather prediction. *J. Comput. Phys.* **80**, 27–60.

Skamarock, W. C. & Klemp, J. B. 1993 Adaptive grid refinement for two-dimensional and three-dimensional nonhydrostatic atmospheric flow. *Month. Weath. Rev.* **121**, 788–804.

Slinn, D. N. & Riley, J. J. 1998 Turbulent dynamics of a critically reflecting internal gravity wave. *Theoret. Comput. Fluid Dyn.* **11**, 281–303.

Smyth, W. D. & Moum, J. N. 2000 Anisotropy of turbulence in stably stratified mixing layers. *Phys. Fluids* **12**, 1343–1362.

Smyth, W. D. & Peltier, W. R. 1990 Three-dimensional primary instabilities of a stratified, dissipative, parallel flow. *Geophys. Astrophys. Fluid Dyn.* **52**, 249–261.

Squire, H. B. 1933 On the stability for three-dimensional disturbances of viscous fluid flow between parallel walls. *R. Soc. Lond. Proc.* A **142**, 621–628.

Thorpe, S. A. 2004 Recent developments in the study of ocean turbulence. *Annu. Rev. Earth Planet. Sci.* **32**, 91–109.

Troy, C. D. & Koseff, J. R. 2005 The instability and breaking of long internal waves. *J. Fluid Mech.* **543**, 107–136.

Venayagamoorthy, S. K. & Fringer, O. B. 2007 On the formation and propagation of nonlinear internal boluses across a shelf break. *J. Fluid Mech.* **577**, 137–159.

Vlasenko, V. & Hutter, K. 2002 Numerical experiments on the breaking of solitary internal waves over a slope-shelf topography. *J. Phys. Oceanogr.* **32**, 1779–1793.

Werne, J. & Fritts, D. C. 1999 Stratified shear turbulence: evolution and statistics. *Geophys. Res. Lett.* **26**, 439–442.

Wolfsberg, A. V. & Freyberg, D. L. 1994 Efficient simulation of single species and multispecies transport in groundwater with local adaptive grid refinement. *Water Resour. Res.* **30**, 2979–2992.

Woods, J. D. 1968 Wave-induced shear instability in the summer thermocline. *J. Fluid Mech.* **32**, 791–800.